UNIVERSITY OF CALGARY

Evaluation of Strategies To Reduce Tribocorrosion of Steel Components

by

Brandon Christopher Wong

A THESIS

SUBMITTED TO THE FACULTY OF GRADUATE STUDIES

IN PARTIAL FULFILLMENT OF THE REQUIREMENTS FOR THE

DEGREE OF MASTER OF SCIENCE

DEPARTMENT OF MECHANICAL AND MANUFACTURING ENGINEERING

CALGARY, ALBERTA

APRIL, 2020

Abstract

In oil and gas applications, such as for rod pumps used in oil extraction, metallic components are often subjected to corrosive environments and simultaneously abraded by sand. This presents a serious problem as wear reduces efficiency and necessitates the replacement of parts, resulting in increased costs. The purpose of this thesis is to examine strategies for reducing tribocorrosion, including boronizing treatment processes for steels, and using friction reducers and chemical additives in pipelines carrying fracking fluid. The tribological behaviour of uncoated samples, coated samples, and pipe segments were examined in sliding under both dry and corrosive conditions. 0.5 M NaCl solution and fracking fluid referred to as high Total Dissolved Solids (TDS) water was used in conjunction with a potentiostat to artificially induce electrocorrosion. Friction coefficients were determined through the use of a home-built linear reciprocating tribometer, and wear coefficients were calculated using an optical profilometer and hardness testing. Additionally, Energy Dispersive X-ray Spectroscopy (EDS) was employed to perform chemical characterisation of tribofilms and corrosion by-products. From the experiments, it was discovered that sample boron-doped boronized steels yielded the lowest friction coefficient ($\mu = 0.189 \pm 0.003$) and lowest pseudo-wear coefficient ($k = [5.38 \pm 0.17] \times 10^{-8}$ MPa^{-1}) in dry sliding. This same coating also showed reduced friction with enhanced corrosion in 0.5 M NaCl as opposed to AISI 1018 steel which had worse friction performance under corrosion. From the EDS studies, a mechanism was hypothesized for the cause of friction reduction for corroding boronized steels; sliding leads to the wearing of a thin oxide film produced during corrosion which then acts as a lubricant or an antiwelding surface. From tests performed on steel pipe segments, it found that DynaRate 6524 was the most effective friction reducer in high TDS water, decreasing friction by 20% while DWP 621 on the contrary hindered friction performance resulting in a 20% increase in friction. DyanRate 6524 did not affect wear rates significantly whereas DWP 621 increased wear. It was also observed that electrically induced corrosion poorly affected the friction performance of DynaRate 6524 friction reducer, however, CalGuard 3100 oxygen scavenger which is meant to inhibit corrosion had no affect on the friction performance of DynaRate 6524.

Acknowledgements

First and foremost, I would like to extend my utmost gratitude towards my supervisor, Prof. Dr. Philip Egberts for his unwavering guidance and support all throughout my Master's studies. I would also like to thank my fellow colleges who devoted their time and energy towards assisting me in performing experiments on the tribometer, doing hardness testing, polishing, and analysing data, including Dr. Jitendra Panda, Carolyn Pethrick, and Winson Say. Also, thank you to those who provided their expertise in corrosion including Yao Yang and Zhouwei Tang from Prof. Dr. Frank Cheng's group and Prof. Dr. Florian Hausen of Forschungszentrum Jülich GmbH. Thanks to my co-supervisor Prof. Dr. Simon Park for allowing me use his Zeta-20 optical profilometer and providing ideas for building a tribometer.

I would like to thank Dr. Eugene Medvedovski of Endurance Technologies Inc. for laying the ground work of the boronizing project, providing me with boronized steel samples, cross-sectioning specimens, and assisting in reviewing my work presented at conferences. I would like to acknowledge Dr. Jesús Reséndiz and Carrie Lin for passing the project down to me at the beginning of my degree and providing the background readings necessary. My sincerest thanks to the graduate students of the Egberts research group for their input and advice along the way, especially Nicholas Chan, Penny (Peng) Gong, and Zahra Abooalizadeh. Finally the warmest gratitude to my closest family and friends who were there during hard times providing me with the love and moral support I needed.

Table of Contents

List of Figures

List of Tables

List of Symbols, Abbreviations, and Nomenclature

Symbol	Definition
α	Charge transfer coefficient
β	Reciprocal of Tafel slope
η	Electrical overpotential
μ	Friction coefficient
ρ	Density
$\frac{da}{dt}$	Corrosion rate
AE	Auger Electrons
AISI	American Iron and Steels Institute
ASTM	American Society for Testing and Materials
ATR	Attenuated Total Reflectance
BSE	Back-Scattered Electrons
CAD	Computer Aided Design
c^*	Concentration of limiting species
${c_o}^*$	Concentration of the oxidizing species in the bulk electrolyte

$c_r{}^*$	Concentration of the reducing species in the bulk electrolyte
$c_o(0,t)$	Concentration of the oxidizing species at the surface of the electrode
$c_r(0,t)$	Concentration of the reducing species at the surface of the electrode
d	Indentation width
DAQ	Data acquisition
EDS	Energy Dispersive X-ray Spectroscopy
ΔE	Potential difference
ΔE_0	Standard potential difference
E_{corr}	Corrosion potential
F	Friction force, Faraday's constant (96,485.3329 C/mol)
F_x	Force in the x-direction
F_y	Force in the y-direction
F_z	Force in the z-direction
ΔG	Gibbs free energy
ΔG_0	Standard free energy
H	Indentation hardness
HV	Vickers Hardness (units)
i	Current density
i_{corr}	Current density at corrosion potential
ISO	International Organization for Standardization
k	Wear coefficient
L	Sliding distance
LRT	Linear Reciprocating Tribometer
M	Atomic mass

n	Valency of reaction
N	Normal force
NIST	National Institute of Standards and Technology
P	Applied load
PID controller	Proportional, Integral, Derivative controller
Q	Reaction quotient
R	Ideal gas constant (8.314 J/mol·K)
RMS	Root-Mean Squared
SE	Secondary Electrons
SEM	Scanning Electron Microscopy
SPM	Scanning Probe Microscopy
T	Temperature
TDS	Total Dissolved Solids
USB	Universal Serial Bus
V	Wear volume
VH	Vickers hardness in kgf/mm^3
VI	LABVIEW Visual Instrument
XPS	X-ray Photoelectron Spectroscopy

Chapter 1

Introduction

1.1 Motivation

Friction is ubiquitous in mechanical systems and plays a pivotal role in how they operate. Sometimes friction is desirable, such as with brakes in automobiles, but at other times it has undesirable effects. According to Holmberg, approximately 20% of the world's total energy consumption is used to overcome friction and 3% is used to re-manufacture worn parts, thus reducing friction is imperative to decreasing associated costs and conserving the environment [1]. From these concerns and curiosities regarding the mechanisms associated with friction and wear, the field of tribology has risen. If advanced tribological technologies are applied, then global CO_2 emissions could be reduced by as much as 3140 Mt over the course of 15 years [1]. Despite these encouraging figures, a single reliable technology has yet to be discovered to address the majority of issues surrounding friction and wear. Sliding metal contacts are some of the most prevalent in mechanical systems mainly because metals are selected for their advantageous mechanical properties, such as high strength and stiffness [2]. Many methods of modifying the surfaces of metals have been employed to reduce both friction and wear including work-hardening, case hardening, and surface texturing methods, each having their own benefits and disadvantages.

Work-hardening methods can reduce wear by increasing surface hardness, however, under certain conditions there has been little to no observed effect on friction performance [3]. Surface texturing methods are often costly given the long manufacturing times and large energy expenditure in producing surface texture patterns making this process not very feasible for large-scale operations [4]. On the other hand, case hardening processes are quite cheap to perform and greatly improve wear properties; boronizing in particular has been found to reduce friction for both dry and lubricated sliding conditions [5–8]. In addition to improving friction and wear of sliding surfaces, boronizing has the additional benefits of preventing attack against acids, alkalis, and molten metals [6, 8, 9]. These properties are highly desirable for a variety of working conditions and industrial applications including downhole oil and gas operations which may feature corrosive fluids, chlorides, sulphates, H_2S, bacteria, and micro-organisms [10–12]. Strategies for modifying the surfaces of materials to reduce friction and wear are only the start; lubrication and altering environmental conditions can also reduce erosive wear and corrosion in given environments [13]. In fracking, friction reducers and other chemical additives are used to change the behaviour of two-phase flow containing liquid and sand/proppants in order to reduce erosion and corrosion on pipelines carrying fracking fluid. The objectives of the work presented in this thesis can be broken down into two parts: the designing and building of a tribometer for measuring the tribological properties of steels in reciprocating sliding, and the evaluation of strategies for reducing friction and wear in both dry and corrosive environments.

1.2 Structure

This thesis is broken down into eight chapters. Chapter 2 presents an overview of the current state of the field of tribology, particularly addressing the relationships for friction and wear at a macroscopic scale, which then leads into a brief definition of corrosion and tribocorrosion. Following this discussion, boronizing of steel, a process which can sometimes be a solution to these aforementioned corrosion and tribocorrosion issues, is explained. More specifically, the applications, manufacturing methods, mechanical properties, and

chemical properties of boronized steel is outlined, followed by an overview of hydraulic fracturing, or fracking. Fracking is one energy extraction process in which significant corrosion, wear, and other processes detrimental to the the infrastructure are present. Chapter 3 provides the design and construction of our home-built linear reciprocating tribometer, entailing the design selection process, components, and electrochemical control via a potentiostat for tribocorrosion tests. This apparatus is the key building block for the measurement, evaluation, and Procedures for dry sliding, tribocorrosion, potentiodynamic polarization, optical profilometry, Scanning Electron Microscopy (SEM), and micro/nanohardness testing are presented Chapter 4 along with details on how friction and wear coefficients are calculated. Chapter 5 shows the results for boronized steels which includes the friction and wear performance in dry sliding experiments, tribocorrosion experiments involving electrochemical corrosion, chemical characterization using Energy-Dispersive X-ray Spectroscopy (EDS), and micro- and nanohardness testing. Chapter 6 presents the tribological tests performed on real pipe segments in what is referred to as "high total disolved solids water" along with the use of two polyacrylamide-based friction reducers was evaluated along with an oxygen scavenger. Finally, Chapter 7 and Chapter 8 conclude the thesis and give conclusions, final remarks, and recommendations.

Chapter 2

Literature Review

2.1 Tribology

The word *tribo* derives from the Greek word τριβω, which translates to "I rub", with tribology being the study of interacting surfaces in relative motion [14]. This branch of science and engineering encompasses friction, wear, and lubrication, all of which are integral to mechanical systems. The technical problems surrounding tribology are seen on a daily basis from the fuel economy of the automobiles we drive to the dulling of knife blades and other cutting tools we use. In fact, it is estimated that approximately 23% (1.19×10^{11} GJ) of the world's total energy consumption originates from tribological contacts, and of that 20% is used to to overcome friction, while 3% is used to replace worn parts [1]. If friction or wear could even be reduced by a small amount, the potential cost savings across multiple industries could be immense. In to order quantify the behaviour of materials in sliding contact, various models have been developed to describe how they interact, most of which are based off of empirical observations. Leonardo da Vinci was the first person known to have performed friction studies with sliding wood blocks pulled by weights [15], and even before lubricants were first employed approximately 4400 years ago by the Ancient Egyptians [16]. From these humble beginnings, humanity has realized the importance of friction along with its scientific nature. Leonardo da Vinci discovered

that the force of friction is invariant of the contact area and proportional to the weight of the block. From these observations, the following canonical relationship describing the force of friction was developed

$$F = \mu N \tag{2.1}$$

where F is the friction force acting in opposition to sliding, N is the normal force acting between the sliding surfaces and μ is a constant known as the coefficient of friction for the sliding surfaces. This primitive model is still used to date due to its simplicity and applicability at the macro-scale, however, the underlying mechanisms of what makes one material slippery versus another are not fully established. Throughout history with regards to the development of machine elements involving moving components, issues surrounding wear have arisen concerning materials selection. The Ancient Egyptians were aware of wear and used copper nail studded rims on wheels for wear reduction, and the Chinese in 255 B.C. used iron rings (bushings) to avoid wood/iron contacts with higher wear rates [16]. It would be centuries before an empirical model for wear would be conceived. Reye's hypothesis formulated in 1860 explained that the consumption of a solid body due to the friction of sliding is proportional to the energy dissipated, thus being related to the applied force [17]. Archard later formalised this into the Archard wear equation

$$k = \frac{HV}{PL} \tag{2.2}$$

where k is the Archard wear coefficient, H is the indentation hardness, V is the wear volume, P is the applied load, and L is the sliding distance [18]. An assumption made by the Archard wear equation is that all asperities (i.e. the contact points between the two sliding surfaces) of the softer body wear at an equal rate across the sliding distance [18]. Measuring both the friction coefficient μ and the wear coefficient k are practical goals of numerous studies. Doing so requires two things: the construction of an instrument for measuring friction, and a way of measuring mass loss or volume loss. Tribometers are devices that

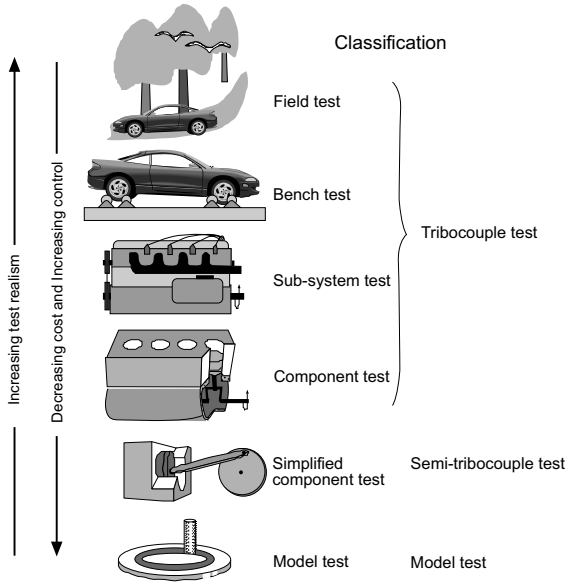

Figure 2.1: Classification of tribotests according to the degree of realism/control [19].

serve the purpose of measuring friction and at least qualitatively observing wear. Various classifications of tribometers are used to achieve different degrees of control and realism for tribotesting [19] as shown in Figure 2.1. Common types of tribometer designs used for controlled model testing in the laboratory include pin-on-disc, and block-on-cylinder, just to name a few. To measure friction, force sensors are used to measured the force in the applied normal direction and the resolved force in the lateral direction that is in opposition to sliding. To measure wear, there are two common practices. If there is a measurable change in mass, especially for tests involving abrasive wear or fretting wear, then this may be a suitable method for determining wear [19]. Otherwise, if wear is mild and the change in mass is not sufficiently measurable, then a profilometer of sorts must be used to optically measure the topography of the surface so as to calculate the change in volume [20]. These tools assist us in making informed decisions when it comes to materials selection for improving tribological performance.

2.1.1 Corrosion and Tribocorrosion

Before discussing tribocorrosion, it is important to first understand the process of corrosion. It is the transfer of a species from that of a high-energy state to a lower energy state (i.e. from a pure metal to a metal oxide). This can be broken down into oxidation and reduction half-reactions that occur simultaneously in an aqueous environment

$$\mathrm{M} \rightleftharpoons \mathrm{M}^{n+} + n\mathrm{e}^{-} \tag{2.3}$$

$$\frac{1}{2}\mathrm{O}_2 + \mathrm{H}_2\mathrm{O} + 2\mathrm{e}^{-} \rightleftharpoons 2\mathrm{OH}^{-} \tag{2.4}$$

where M is the metal species and n is the valency of the reaction (usually $n = 2$ for iron). When Equation (2.3) and Equation (2.4) are combined, they are referred to as an oxidation-reduction (redox) reaction. In order for corrosion to occur, conditions must be thermodynamically favourable as dictated by Gibbs fundamental equation [21]

$$\Delta G = \Delta G_0 + RT\ln(Q) \tag{2.5}$$

where ΔG is the Gibbs free energy, ΔG_0 is the standard free energy, R is the ideal gas constant (8.314 J/mol·K), T is temperature, and Q is the reaction quotient of the reaction $a\mathrm{A} + b\mathrm{B} \rightleftharpoons c\mathrm{C} + d\mathrm{D}$ for which

$$Q = \frac{[\mathrm{C}]^c[\mathrm{D}]^d}{[\mathrm{A}]^a[\mathrm{B}]^b} \tag{2.6}$$

If $\Delta G < 0$ then the reaction is spontaneous. However, in addition to the energy associated with enthalpy and entropy of the chemical reaction, there is also the energy associated with the separation of charge or capacitance created at the interface of the metal species and aqueous environment. As ions migrate and electrons tunnel to the surface of the metal, a passivating oxide layer develops which begins to inhibit

corrosion. Thus in considering the electrical energy and chemical energy which are equal to each other in magnitude at equilibrium, this gives rise to the Nernst equation [22]

$$\Delta E = \Delta E_0 + \frac{RT}{nF} \ln(Q) \tag{2.7}$$

where ΔE is the potential difference between the two half-cells, ΔE_0 is the standard potential difference of the cell, R is the ideal gas constant, n is the valency of the chemical reaction, F is Faraday constant (96,485.3329 C/mol), and Q is the reaction quotient described earlier in Equation (2.6). This provides us with the electrochemical series that describes the preferentiality of one metal to corrode versus another based on its electrochemical potential (E_{corr}). However, this does not provide details on rates of corrosion nor of the behaviour in the development of passivating oxide films that inhibit corrosion which depend on numerous factors including crystallographic orientation, defects, grain boundaries, alloying etc. [23, 24]. These rates must be determined experimentally by performing electrochemical tests which involve applying a potential (E) between the environment and given metal as to artificially induce corrosion. Faraday's law of electrolysis dictates that that the corrosion rate is proportional to the current coming off of a sample [25]. If the reduction or oxidation reaction is known, corrosion rate can be determined using the following equation

$$\frac{da}{dt} = \frac{iM}{nF\rho} \tag{2.8}$$

where da/dt is the corrosion rate in terms of length per unit time, i is the current per unit area flowing through the metal at the exposed surface, M is the atomic mass of the metal, n is the valency of the reaction, F is Faraday constant, and ρ is the density of the metal. Faraday's law is particularly useful in combination with the Tafel's equation which empirically describes the electrochemical kinetics as a logarithmic function of the electrical overpotential [26]

$$\eta = E - E_{\text{corr}} \tag{2.9}$$

$$= \frac{1}{\beta} \ln\left(\frac{i}{i_{\text{corr}}}\right) \tag{2.10}$$

where η is the electrical overpotential, A is the Tafel slope (sometimes $1/\beta$ is substituted for A), i is the current per unit area flowing through the metal, and i_{corr} is the current per unit area flowing through the metal when there is no overpotential ($E = E_{\text{corr}}$). As mentioned at the beginning of this section, corrosion involves two competing half-reactions – oxidation and reduction. The more positive the overpotential the more dominant the oxidation half-reaction will be, and the more negative the overpotential the more dominant the reduction half-reaction will be. Tafel's equation only applies when $|\eta| \gg 0$, thus it can be used to generate two curves, one for each half-reaction. The anodic curve, which is dominated by the oxidation half-reaction, is usually of the main concern. It should be noted that the Tafel equation is only applicable under the conditions that the electrochemcial reactions are activation controlled – that is the electrode potential purely dictates the reaction rate. However, if the redox reactions are diffusion controlled given that the flux of reactants at the electrode surface are the limiting factor, then the current is instead

$$i_{limiting} = \frac{nFD}{\delta c^*} \tag{2.11}$$

where D is the diffusion coefficient, δ is the diffusion layer thickness, and c^* is the concentration of the limiting species in the reaction. This leads to the general form of the Bulter-Volmer equation along with the modified polarization equation

$$i = i_0 \left(\frac{{c_o}^*(0,t)}{c_o} e^{-\frac{\alpha n F \eta}{RT}} - \frac{{c_r}^*(0,t)}{c_r} e^{\frac{(1-\alpha) n F \eta}{RT}}\right) \tag{2.12}$$

$$E = E_0 + \frac{RT}{nF} \ln\left(\frac{i_a(i_c - i)}{i_c(i_a - i)}\right) \tag{2.13}$$

Without going into too much detail on the derivation of the equations, the concentration of the oxidizing and reducing species both at the surface ($c_o(0,t)$, $c_r(0,t)$) and within the bulk of the electrolyte ($c_o{}^*$, $c_r{}^*$) over time (t), and the charge transfer coefficient (α) now play a role in determining the potential and current density flowing through the metal. Also, there is a limit to the amount of current which can flow through the metal when polarized to either extreme such that $i = i_c$ when E approaches $-\infty$ and $i = i_a$ when E approaches ∞.

When combining the effects of both degradation due to wear (which is a physical process) and corrosion (which is a chemical or electrochemical process), we get the phenomena known as tribocorrosion. In mechanical systems, the effects of one or the other may be present, but when combined the effect may be greater than when they are considered individually. This is due to complex synergistic and antagonistic effects of stress-activated chemical reactions and redepositing of wear debris that take place to form tribofilms [27, 28]. These tribofilms create a third body which changes the contact pressure and interaction of sliding surfaces, thus leading to tribofilm evolution [27, 28]. Additionally, the continuous mechanical removal of passivating films that may be formed and would otherwise inhibit corrosion results in unique tribological behaviours [29–32]. This can lead to changes in friction coefficient which have been observed for steel alloys [33]. To study the effects of tribocorrosion, one uses a tribometer equipped with an electrochemical cell that can impose electrical potentials meant to regulate the rate of corrosion. If we recall, going back to where we left off at explaining corrosion, knowing the redox reaction and overpotential it is possible to draw conclusions regarding effect of corrosion on the rate of mechanical wear by subtracting the volume loss due to corrosion from the total volume loss over the period of testing. Studying the effects of tribocorrosion is important as the effects can be lead to drastic changes in tribological performance.

2.1.2 Erosion corrosion

With regards to tribocorrosion, erosion corrosion is a more narrowly defined processes that describes the degradation of material due to multi-phase flow enhanced dissolution. Sand and other particles in fluid flow remove the protective oxide film of a substrate which can cause high pitting rates, accelerating corrosion. Erosion corrosion is a fairly common challenge in the oil and gas industry, threatening the integrity of pipelines, especially in the cases of extracting resources from wells during the process of hydraulic fracturing. When sand is transported in a slurry through pipelines for hydraulic fracturing, the interior surface is abraded and worn away, revealing fresh steal underneath the rusted surface resulting in significantly higher rates of corrosion than normal. The mechanisms behind erosion corrosion are not fully understood given the large number of parameters that influence the process (such as flow rate, impingement angle, particle size, surface roughness, temperature, concentration, pH, etc.), but several studies have attempted to use either physical flow loop models [34, 35] or Computational Fluid Dynamic (CFD) models [36, 37] to observe the effects of erosion corrosion. In pipelines containing fracking fluid, the motion of particles applies both erosive and abrasive wear as shown in Figure 2.2. Particles of sand flowing through the pipe at high velocities, due to the immense pressure used to fracture rock formations, may slide along the bottom surface while being pressed due to the weight of the fluid. This leaves long narrow wear tracks which can be emulated by the sliding of a very small contact such as that of a sphere. With this prior information, some studies have attempted to apply a pin-on-disc or reciprocating tribometer as to model the tribological conditions of erosion imposed by multi-phase flow in a controlled manner [38]. Whether this is accurate has yet to be proven given the challenge of attempting to determine the mean contact pressure exerted by sliding particles against pipe walls in fluid flow.

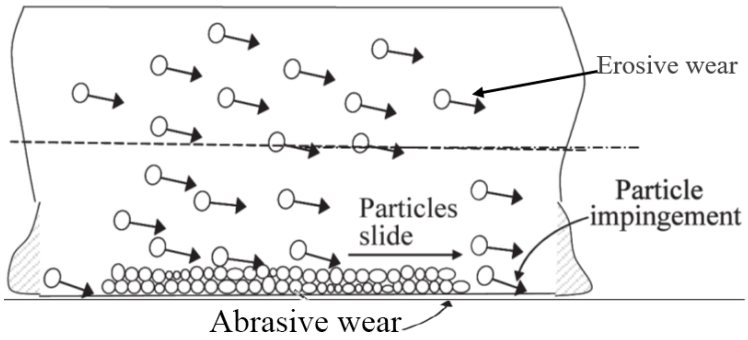

Figure 2.2: Schematic of the abrasive and erosive wear processes that occur in steel pipes used in hydraulic fracturing.

2.1.3 Measuring tribocorrosion

Given the damaging nature of erosion corrosion, scientists and engineers have been tasked with developing methods of measuring erosion corrosion. Quantifying the amount material removed through erosion corrosion without using computer models is usually accomplished by monitoring mass loss or volume loss. By using an apparatus such as a tribometer – a device which can control mechanical wear and/or electrochemical parameters – controlled experiments can be conducted after which a scale or optical profilometer can be used to evaluate the total amount of material removed due to both mechanical and electrochemical means. In order to isolate each component, electrochemical analysis is performed in order to determine the amount of galvanic current flow. Using this in conjunction with Faraday's law of electrolysis Equation (2.8), the amount of material removed due to corrosion can be extracted.

2.2 Surface Modification through Boronizing

In tribology, a number of manufacturing methods have been employed in order to address friction and wear, from mechanical methods of work-hardening such as rolling, shot-peening, laser peening, and ultrasonic electropulsing, chemical methods of case hardening such as carburizing, nitriding, and cyaniding, to surface texturing methods such as micro-machining, electrochemical texturing, laser texturing, and photochemical machining. There are advantages and disadvantages to each method, both in terms of cost and scalability.

Surface texturing methods are effective at reducing friction (and sometimes also wear) by decreasing the true contact area between surfaces [39]. However, they can take a long time to perform, consume a fair amount of energy, and consequently are not easily scalable processes [4]. Methods that involve work-hardening of the surface can possibly reduce wear by increasing surface hardness. However, there are limitations to the amount of work hardening that can be performed on a given component since the total remaining deformation available is reduced, and work-hardening tends to only affect wear performance having little to no effect on friction performance in certain circumstances [3]. Case hardening methods on the other hand are relatively inexpensive and can be combined with work-hardening to further enhance the tribological properties of materials [40]. In this thesis we will examine the tribological performance of thermal diffusion boride coatings for steels. Boronizing/boriding in itself is not a novel technology with its mechanical properties having been documented as far back as 1959 [41]. Boronizing is like any other surface hardening process in that boron is diffused into the surface layer of a workpiece at elevated temperatures (usually above 850°C). By controlling various parameters such as the concentration of gases pumped into the furnace, heat treatment temperature, time, cooling etc., different effects can be achieved that alter the microstructure and lead to different properties. The reason why boronizing is such a promising technology is the multiple benefits it has to offer; from early studies, the high hardness and acid resistance of boride coatings have been examined and used to prevent both abrasive wear and chemical attack, and can be applied to a variety of steels and alloys [42].

2.2.1 Applications

For operations that take in oil wells below ground, commonly referred to as downhole operations in the industry, many components, such as sucker rod pumps used for the extraction of oil. These pumps operate on the principle that a reciprocating rod moves in a cylinder. These rods in particular need to be protected from damage associated with sliding abrasion coupled with harsh environmental conditions. In the case of

sucker rod pumps, they undergo continuous reciprocating motion in operation which results in issues with several components of the pump failing on a regular basis [43]. Due to misalignment between the moving metal surfaces, such as between tubing and casing components, as well as the addition of sand and fine silica particles drawn along with oil during the extraction process, severe wear can arise at the surfaces in contact. This issue is only further exacerbated by high contact pressures experience when sand is pressed into the surfaces, and corrosion from fluids that are often present which may include chlorides, sulphates, H_2S, bacteria, and micro-organisms [10–12]. These are potentially some of the worst conditions experienced by steel components in sliding. For other engineering applications besides down-hole oil and gas, friction and sliding abrasion conditions are prevalent elsewhere, and many metallic components could benefit from boronizing to increase their lifespan. Successful applications of boronization in reducing wear have been seen in cutting blades for tobacco which last 25 times longer, grinding disks for coffee roasting plants which had a five-fold increase in service life, feed water regulating valves which lasted 9 times longer without exhibiting such advanced wear, oil burner nozzles, punch dies, forging dies, pawls, railcar suspension parts, gears in diesel automobiles, pipes carrying PVC, and cone drilling bits for mining [42]. Such drastic improvements in wear reduction for multiple applications are promising, especially when considering the economical nature of producing boronized components.

2.2.2 Manufacturing Methods

The processes of boronizing the specimens examined in this thesis are based on the principles of Chemical Vapour Deposition (CVD) [44]. Being analogous to other thermochemical processes such as carbonizing and nitriding, boronizing involves the deposition of boron and other select elements onto a preheated workpiece with consequential chemical modification of the metal surface through the formation of a new hard inorganic phases [45]. These inorganic phases diffuse and grow into the substrate becoming integrated into the microstructure such that there is no mechanical interface between the coating and substrate, therefore having

no possibility of delamination. Boronizing can be performed with active vapours/gases such as diborane, liquid compounds, or solid compounds and pastes [42]. This process maintains tight dimensional tolerance of the workpiece without the need for machining afterwards [5]. There are two underlying chemical reactions that form iron borides

$$B + Fe_2B \rightarrow 2FeB \tag{2.14}$$

$$B + FeB \rightarrow Fe_2B \tag{2.15}$$

Depending on heat treatment and time, either a single layer of Fe_2B, or a double layer of Fe_2B on the interior and FeB on the exterior with a sawtoothed morphology can be produced. Figure 2.3 shows a cross-section of boronized low-carbon steel (AISI 1018), revealing an iron boride double layer. The rate of diffusion heavily controls the development of the microstructure in the reaction zone which follows a parabolic behaviour [46]. Tuning these parameters has been the focus of many scientists and engineers in order to achieve compatible coatings with good tribological and corrosion performance. Endurance Technologies Inc. makes the boron thermal diffusion steel specimens used in this thesis and have a vested interest in improving the formulations of their coatings; they are not transparent on the details of their manufacturing processes, however, Table 4.1 provides as much information as is made openly available. Studies have been performed showing that boronizing can be applied effectively to not only low-carbon steel, but also other steels and alloys such as high strength steels such as AISI 52100 and N80 tube steel, cast irons, stainless steel alloys such as AISI 304 and AISI 316L, nickel-based alloys such as Inconel 625 and Inconel 718, and Titanium alloys such as Ti-6Al-4V [6–9, 42, 47]. Since this processes is economical and straightforward, it can be applied to numerous metallic components of various sizes, geometry, and composition [9].

Figure 2.3: *On the left* an optical image of the microstructure of boronized low-carbon steel (AISI 1018), and *on the right* a schematic describing the various layers [6].

2.2.3 Mechanical Properties

Zhigach studied ways of boronizing steel with volatile boron compounds – mainly based off of the preliminary work of chemists examining boron-trialkalis to boronize metals – to produce high hardness steel. From their findings, it was reported that "a very hardboronized case, 200 microns (0.008 in) thick, was obtained on [carbon] steel 45; the surface microhardness was 3000" [41] ; the hardness scale used here is unclear. However, subsequent studies have indicated that the hardness of the iron boride layers on various types of steels are typically around 1500 HV [5–8]. Only a few thousandths of an inch in case depth is required to form a new phase on top to drastically improve the surface hardness of metal components. Since the innate hardness of the iron boride layers is only present at the surface, the mechanical of the bulk material remain unchanged. Thus a tensile test would be ill-suited for testing the mechanical properties of the coating – instead we must resort to making indents on coating. By analysing the size of the indents produced by an indenter of known geometry, the local plastic deformation can be determined indicating the hardness of the material. Section 4.7 later provides more details regarding how these tests are performed on the coatings. Boronized steels are evidently highly resistant to abrasive wear, adhesive wear, and erosive wear due to their high hardness [5,6,48]. As mentioned, the properties of the bulk material are unchanged post-boronization, this is often advantageous

as materials are selected for applications based on their bulk properties.

2.2.4 Chemical Properties

In addition to the high hardness of boronized steels, its chemical properties have proven to be beneficial against simultaneous erosion wear and corrosion. Bronized steels have been noted to be highly resistant to attack from non-oxidizing dilute acids such as hydrochloric acid, alkalis, and molten metals such as zinc [6,8,9]. Because of the relatively inert nature of boride coatings, they are of interest for tribocorrosion studies. At this time, not much is known regarding what reactions take place in corrosive environments and the mechanism that reduce wear, especially under the high contact pressures produces by rubbing asperities. What is known is that boron has a high affinity for oxygen, thus borides tend to form oxide films which may be the source of many of their desirable properties [9].

2.3 Hydraulic Fracturing

Fracking, otherwise known as hydraulic fracturing, is a technique for stimulating oil and gas wells as to extract fossil fuels from rock formations. This involves injecting high-pressure liquid known as fracking fluid – primarily water containing sand/propprants along with chemical additives – into boreholes as to fracture and expand rock formations thus allowing for the release of fossil fuels and brine. Once hydraulic pressure is alleviated, the cracks remain open due to the sand/proppants that are embedded [49]. Figure 2.4 shows how natural gas is extracted via fracking. Cracks generally emanate perpendicular to the horizontally drilled borehole. Because fracking operations typically take place at depths around 1.6 km to 3.2 km, the pressures that are needed in order to overcome the tensile strength of the rock along with the weight of the overlying strata are close to 100 MPa [50]. Thus, a constant supply of fracking fluid is necessary to maintain these pressures. As mentioned, fracking fluid is composed primarily of water with sand, but is also mixed with brine and other chemical additives that serve many purposes: they can keep proppants suspended, provide

lubrication, tune viscosity, promote gel formation, alter pH, reduce dissolved gas content, prevent corrosion, inhibit microbial growth, delay breakdown of polymers, lower the freezing temperature etc. [50, 51]. Besides what original fracking fluid is pumped into the rock formations, fluids known as flowback are returned to the surface and collected. Flowback may comprise 3% to 80% of the total fluid used to fracture the well and contains additional minerals from the fractured rock formation [52]. There are strict regulations for the management of fluid waste in North America as to protect surface and ground water aquifers. As of now the most common practice for disposing of waste flowback is to store it in permitted and monitored injection wells [52]. Pipes that transport both fracking fluids and flowback containing sand and additives are subjected to erosion and also corrosion. This leads to the issue of thinning of pipe walls to the point where they are eventually unable to sustain the high-pressures and must then be replaced. Hence, improving the service life of these pipes through tribocorrosion studies in laboratory conditions are of interest for oilfield service companies involved in fracking operations such as CalFrac Well Services. Certain chemical additives could alter their tribological performance. Additionally, water management is a serious issue with regards to preventing noxious chemicals in fracking waste water from leaching into and contaminating surrounding aquifers [51, 53]. By discovering which chemicals can be used in the lowest concentrations to solicit the best tribological performance, environmental impact can be reduced. CalFrac is currently looking into the use of anionic and cationic water-soluble polymer friction reducers to provide improved proppant transport to reduce wear, and oxygen scavenging agents to inhibit corrosion on their pipes carrying fracking fluids.

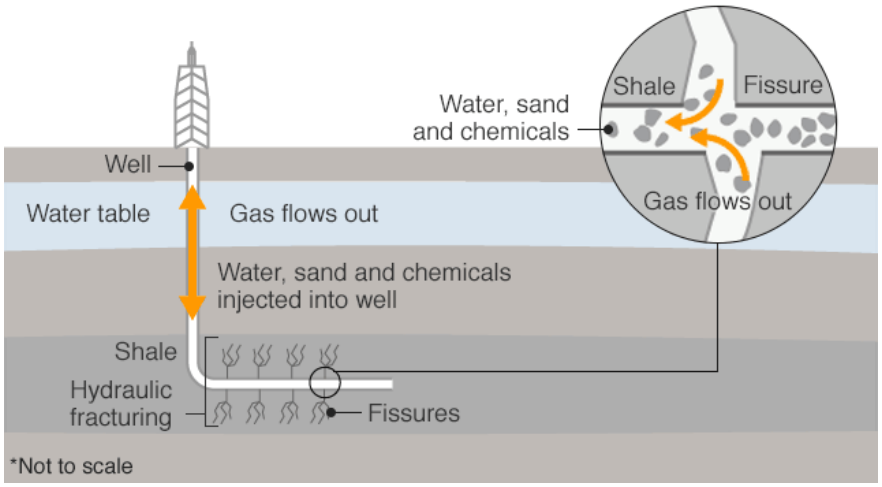

Figure 2.4: Illustration of the fracking process used to extract natural gas from shale rock formations [54]

Chapter 3

Tribometer Design and Construction

This chapter describes the design, operational parameters, and theoretical considerations in making a reciprocating tribometer with control over electrochemical corrosion. The final design for the tribometer that was constructed at the University of Calgary is included within this chapter within this chapter in sufficient detail that a replica copy could be made in the future. The chapter is organized such that the theoretical design and operation of a reciprocating tribometer is first described. Following this description, the construction of the tribometer is detailed, first outlining the individual components used in building the tribometer, followed by the technical drawings and assembly information for the tribometer. Finally the functions of the computer code use to operate the tribometer are discussed in this section. In the final section of this chapter, the design of the electrochemical cell used in tribochemical measurements are included.

3.1 Motivation

To investigate tribological properties and predict wear or energy loss in mechanical systems involving the sliding of surfaces, suitable instruments and models must be developed to simulate real world conditions but in a much more controlled manner. As discussed previously in a brief introduction to tribology, instruments known as

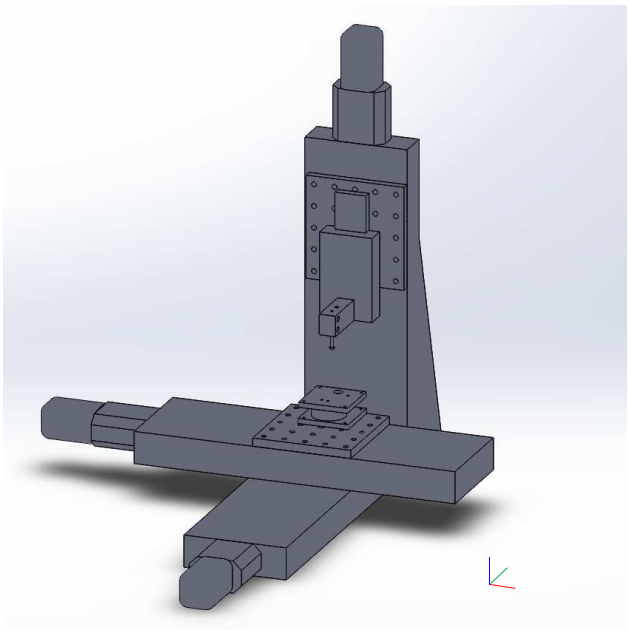

Figure 3.1: View of our home-built linear reciprocating tribometer designed in SOLIDWORKS. x, y, and z-axis of motion are defined by red, green, and blue lines respectively and are 25 mm in length each.

tribometers are developed specifically for the purpose of measuring these properties. Because many mechanical systems have various components that transfer energy, observing the effect of altering one component of a given system may not be feasible, nor does it provide direct insight into the underlying mechanisms that influence the tribological properties. Through constructing a tribometer rather than purchasing one commercially, a greater understanding of the factors of experiments can be achieved. Ostensibly, there are many variables of mechanical system, but only a portion of those may significantly contribute to sliding behaviours and phenomena – at least at the observable scale of the system. For this thesis, a large portion of the work went into construction of a linear reciprocating tribometer which was foundational to the following experiments. Without managing the designing and resourcing of components of the tribometer, progress towards completing all the desired experiments would not have been possible.

3.2 Linear Reciprocating Tribometers

Linear reciprocating tribometers (LRT) are instruments used to characterize the tribological performance of various materials and lubricants. In real mechanical systems, many translational mechanisms often undergo linear reciprocation motions, which can be simulated by a LRT [55]. Additionally, the reciprocative motion of LRTs allows for a greater precision in the determination of wear compared with other devices used to measure friction, such as pin-on-disc tribometers which often yield lower wear than predicted [19]. These two tribometers are the most typical instruments used to characterize lubricant performance and wear of sliding interfaces. Figure 3.2 (a) and (b) contrast the configurations of a LRT and a pin-on-disc tribometer, respectively. In a LRT, a sample is translated beneath a fixed counter surface made of a material that is inert and harder than the sample. The counter surface is pressed against the sample at a given normal force, which can be measured with a force sensor either beneath the sample or above the counter surface. The sample is then translated in one direction at a given constant velocity while the counter surface is held at a rigid position. Simultaneously the lateral force, or the instantaneous force acting in the direction opposite to the motion of the sample is measured, while sliding occurs. After a pre-determined distance has elapsed during the sliding experiment, the sample is stopped, and then slid in the opposite direction for the same distance and velocity as was performed in the first stage of the measurement. Under a constant normal force, the lateral force is once again measured during this period. Following the completion of this reverse displacement, the stage is stopped. This series of concerted displacements then constitutes one complete cycle. Following this first cycle, the measurement is repeated over and over again for the desired number of cycles. The friction force for a single cycle can then be determined by averaging the lateral force in the forwards and reverse directions, and the friction coefficient can then determined by taking the average friction force during this one cycle and dividing it by the average normal force measured during the cycle. This determination of the friction coefficient has the advantage of being able to remove the influence of any misalignment between the normal of the sample surface and the direction of the applied normal force resulting from the angle at which

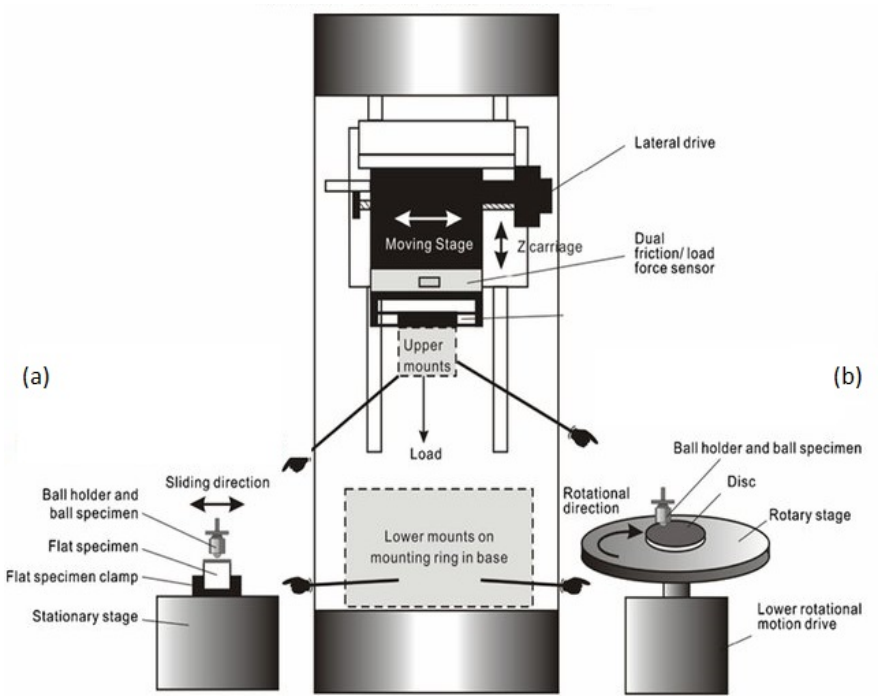

Figure 3.2: Comparison of the configurations of a LRT and pin-on-disc tribometer [59].

the counter surface contacts the sample surface, and also aids in measuring low coefficients of friction [56, 57]. One disadvantage of the LRT is that translation speeds are often slow (mm/s or lower are typical), resulting from the requirement that the sample must be accelerated and de-accelerated at the beginning and end of the forward and reverse cycles. Thus LRTs are often unable to achieve elastohydrodynamic lubrication regimes of lubricated contacts [58]. On the other hand, this slow repetitive motion makes controlling and containing fluid lubricants or analytes easier than if the sample was translated faster, such as in a pin-on-disk tribometer.

A pin-on-disc tribometer is illustrated in Figure 3.2 (b). In this tribometer, the sample is often shaped in a disk and rotated beneath the counter surface, which is pressed into the disc at a constant normal force. Normally, the disc is rotated in a single direction for the entirety of the measurement time, allowing very high sliding speeds to be achieved (tangential velocity at the contact point between the sample and the counter surface are typically m/s or higher), as the turning motion in the LRT is eliminated. As the speed can be easily varied from very slow to very fast (μm/s to m/s), the variation of a lubricant's performance over a wide range of sliding speeds and applied normal forces can be measured, which is critical in developing what

is called a Stribeck curve [60]. As the motion of the sample may be less controlled during a pin-on-disc measurement, the number of passes or instances that the counter surface slides over a specific region of the sample may be more difficult to determine. Furthermore, pin-on-disc measurements are more sensitive to correct alignment of the sample normal and the applied normal force by the counter surface and variability in sample height over the disc, as there is no reverse motion that can be easily performed to remove this influence. Finally, at high rotational speeds, any fluid lubricant or analyte will be pushed to the edges of the disk, or be eliminated from the measurement completely, due to the high centripetal forces experienced by the rotating sample/liquid.

As stated in Chapter 1, the objective of this thesis is to measure the impact of reciprocating sliding on the performance of uncoated and coated steels under dry and corrosive conditions. As such, a LRT was chosen as the optimal setup for friction testing, as it allowed for:

1. Precise control of the number of reciprocations along the sample surface. This control allows for facial determination of wear coefficients.

2. Precise monitoring and adjustment of the applied normal force during each half-cycle.

3. Easy control of liquid flow and access of liquid at the contacting point between the sample and the counter surface.

Aside from the works contained within this thesis, the construction of a linear reciprocating tribometer would be helpful for characterizing other materials in the future given its versatility. The next section describes the considerations made in selecting the various electronic and mechanical components in the the developing the tribometer.

3.3 Tribometer Components

To establish a framework for developing a tribometer design, the publications of various tribologists were studied in an attempt to replicate some of their instruments. With rough diagrams, component specifications, and sliding speeds, a plan was conceived for the type of linear reciprocating tribometer that would be used for the experiments with boronized steels. Dr. Gregory Sawyer's group has much experience with constructing these instruments from scratch, thus their work on uncertainty analysis for low friction measurement was valuable for developing of code to analyse the raw data from the tribometer [56]. This entire process took the greater part of 6 months to achieve an operational LRT which could then be used for subsequent experiments.

3.3.1 Linear Actuators

Three linear actuators were used in the design in the tribometer pictured in Figure 3.1. One translates the sample in the x-direction, which is the reciprocation direction during friction measurements. One translates the sample in the y-direction, allowing for automated repositioning of the sample-counter surface contact during multiple friction measurements. Finally, one linear actuator is used in the z-direction, with allows for the counter surface to be approached to the sample, as well as for controlling the normal force applied on the sample by the counter surface with closed loop feedback.

When selecting the linear actuators, the following qualities were desired:

- *Little to no backlash.* This quality ensures that once the movement of the stages was completed that it did not move, thus allowing for precise control of the applied normal force (through actuation of the z-linear actuator) without constant feedback during the reciprocation motion.

- *Stepper motor controlled displacement.* Traditional direct current motors with an armature coil have little to no control over the distance that the actuator will move (at least without an encoder), as the amount of displacement depends on the current applied to the motor and the resistive force against the

movement. Stepper motors on the other hand allow for an exact measurement of the rotational output of the motor (which corresponds to the number of steps the motor makes).

- *Embedded micro-controllers.* Embedded micro-controllers in the linear actuator allow for facile interfacing of the linear stages with control electrons. Additionally, most linear actuators that contain a micro-controller have the ability to measure the distance by which the actuator was displaced during the control sequence.

- *Sufficient Displacement Range.* Linear actuators have the ability to move in variable ranges. In particular, larger displacement actuators that move under the control of stepper motors may have jerk-type motions, depending on the number of magnets contained within the stepper motor and the number of phases/steps per revolution. For linear actuation of the samples during friction measurement, a smooth displacement of the sample is desired so as to not interfere with the measurement of the lateral forces. Sufficiently large reciprocation distances were required so that a sufficient portion of the wear scar was produced at a constant velocity and thus be easily visually identified and have a consistent cross-section.

To meet these design specifications, we chose to use linear actuators from IntelLiDrives with 200 mm of travel. Three drives were mounted in orthogonal directions to allow for 3-axis positioning and displacement of the sample. These actuators use a precision ball screw that provides exceptional accuracy, repeatability, and ultra-fine positioning resolution down to 1 μm. Furthermore, the actuators contain a brushless, direct-drive servomotor that can translate the stage at speeds of up to 100 mm/s. The linear actuators had integrated motors within a housing directly attached to the stage, which also included an encoder, amplifier, and controller which interfaces with a computer through USB. These linear actuators also came with software which allows for programming and control via LabVIEW. Finally, this particular brand of motor contained additional functionality that allowed for manual control of the stages without the computer, to allow for easy coarse positioning of the sample and counter surface at the onset of experiments. Specifications of the linear

translator relevant to the operation of this tribometer are as follows:

- Maximum Translation Distance: 200 mm
- Maximum Acceleration: 10 m/s^2
- Maximum Velocity: 100 mm/s
- Minimum Step Size: 1/800 mm
- Repeatability: < 5 μm
- Maximum Applied Force: 78.48 N (8 kgf)

In addition to being able to be controlled from a computer via a custom user interface designed in LabVIEW, bi-directional rocker switches attached to the microcontroller of each stepper motor can be used to manually control the position of the linear actuators. The linear actuators move with a trapezoidal velocity profile; that is they start from an initial low speed, accelerate linearly up to their nominal high speed, and then decelerate linearly. This reduces the wear and tear on the moving components due to sudden changes in inertia. Although there were other options for providing more precise actuation when selecting components, the linear actuators that we finally decided on using for our tribometer provided the needed accuracy at reasonably high sliding speeds, along with being relatively inexpensive.

3.3.2 Force/Torque Sensor

As stated earlier, one of the requirements of the LRT is to measure the forces applied by the counter surface on the sample, as well as lateral forces. A strain gauge load cell is often selected for use in tribometers. By converting strains into changes in resistance in a load bearing Wheatstone bridge circuit, voltages are able to be measured which through a set of calibrations can then be translated into force readouts. We anticipated that the load applied to the surfaces would be in the mN to N range, with μN resolution desired if possible.

We also wanted to have the possibility to reuse the sensor for a pin-on-disc tribometer for future projects outside the scope of this thesis, thus the ability to measure torque was also desired. Finally, we anticipated that measurement acquisition speeds up to kHz or above would be necessary to achieve a sufficient number of acquired data points within 1/2 reciprocation to measure transient phenomena during a single stroke.

These design requirements were met and exceeded with the ATI Mini40-E transducer. One specific advantage of this force sensor was its small footprint that allowed for attachment of the force sensor to the selected linear actuators. This transducer is most commonly used in applications for robotics and automation is can easily be mounted on manipulable robotic arms. However, to integrate this force sensor with the linear actuators and to attach it to the sample, thus allowing for facile sample exchange, a custom mount was required and is detailed in the subsequent subsection. Out of the box, the sensor came per-calibrated by the seller in compliance with ISO 9001 traceable to the the National Institute of Standards and Technology (NIST). No details were provided on the drift rate of the raw voltage readouts was provided by the manufacturer, however, during our experiments the temperature of the room was kept well within the normal operating temperature range. The specifications relevant for the tribometer are given below:

- Force Range: $F_x, F_y = \pm 20$ N; $F_z = \pm 60$ N
- Force Resolution: $F_x, F_y = 1/200$ N; $F_z = 1/100$ N (effective resolution can be improved with filtering)
- Measurement uncertainty: $F_x = 1.25\%$; $F_y = 1.00\%$; $F_z = 0.75\%$ (with a 95% confidence level as a percentage of the full-scale load at 22.2° ±1.1°C)
- Maximum sampling rate: 10 kHz
- Amplified Output Voltage Range: ±10 V
- Weight: 0.0499 kg
- Diameter: 40 mm

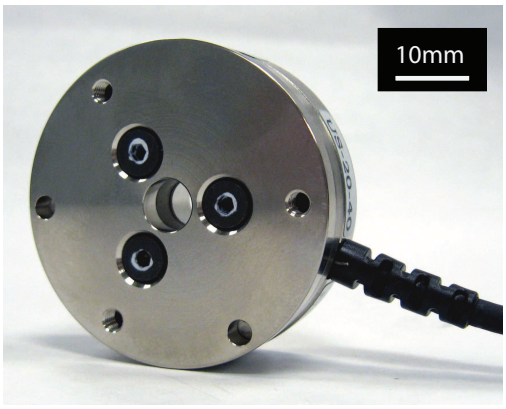

Figure 3.3: Mini40 force/torque transducer [61].

- Height: 12.2 mm

3.3.3 Force/Torque Sensor Mount

Out of the box, the Mini40 force/torque transducer did not include any accessories for mounting it to any surfaces, therefore a custom mount had to be designed. It was highly critical that there be no play at all and very little compliance in the design of the mounts. From Computer Aided Design (CAD) drawings of the sensors provided by the manufacturers, there were two slip fit holes and a M3 threaded hole on both sides of the sensor. A single block of steel was machined flat, then a couple dowels were inserted to interface with the slip fit holes, and a countersink was created to allow a shortened M3 screw to secure the mounts to either side of the sensor.

3.3.4 Data Acquisition

The analog signals from the force sensor were recorded by the control computer at 500 Hz, allowing for over 2000 samples per reciprocation cycle. A National Instruments USB-6363 DAQ was available within the lab for use on the system. This DAQ has maximum sampling frequency of 2.2 MHz and the ability to acquire 32 distinct analog signals simultaneously with a 24-bit resolution. This DAQ is also easily integrated with any computer, as it is attached to the computer through USB. Finally, this DAQ is produced by National

Figure 3.4: National Instruments USB-6363 DAQ [62].

Instruments, and thus can be controlled through LabVIEW.

3.3.5 Passive Vibration Isolation

The tribometer is sensitive to displacements of the sample and counter surface. Thus, isolation of the sample, counter surface, force sensor, and other components of the LRT from vibrations of the building is required. To achieve this, the tribometer was mounted on an optical breadboard attached to a passive vibration table. This set up has mild intrinsic damping and while providing good rigidity for mounting components. The resonant effects of the linear actuators was examined by performing a spectral transformation on the transducer readings over two cycles, and the effect of such vibrations was found to be negligible; looking at the power spectral density, the 0 Hz component was found to have over 1000 times the power of the resonant frequencies at 152 Hz and 347 Hz.

3.3.6 Stylus Counter Surface

For all experiments, a 6 mm optical-grade sapphire hemisphere attached to a hardenned high-carbon steel rod was used as the counter surface, purchased from Edmund Optics. The hemispherical geometry of the sapphire allowed for the formation of a single asperity contact between the counter surface and sample.

The high hardness (1365 HV) of the sapphire counter surface also allowed for most, if not all of the wear occurring during linear reciprocating experiments to be localized to the sample, rather than the counter surface. However, the high stiffness of the counter surface also resulted in a very small contact area. Thus, typical contact pressures for most experiments where Newton loads were used resulted in applied pressures on the order of approximately 1 GPa to 2 GPa, estimated using Hertzian contact mechanics equations which are applicable to the scale of these experiments [63, 64]. Equation (3.1) and Equation (3.2) were used for modeling the maximum contact pressure $P_{\max}$ between a sphere and half-space, where P is the applied force, R is the radius of the half-sphere, E_1, E_2 are the elastic moduli, and ν_1, ν_2 are the Poisson's ratios associated with each elastic body [63]. Beyond the high hardness of sapphire, this material dissipates heat quickly [65], and is also relatively inert making it resistant to corrosion.

$$P_{max} = \frac{1}{\pi}\left(\frac{6PE^{*2}}{R^2}\right)^{\frac{1}{3}} \tag{3.1}$$

$$\frac{1}{E^*} = \frac{1-{\nu_1}^2}{E_1} + \frac{1-{\nu_2}^2}{E_2} \tag{3.2}$$

3.4 Computer Control of LRT

For all experiments, it is critical that the applied normal force remain constant during sliding. Therefore, as material wears – both the sample and countersurface – it is necessary to adjust the relative position of the two which calls for closed loop control. The first idea was to estimate the elastic modulus of the surface versus depth with an preliminary loading test and then use an established relationship to predictively adjust the vertical position of the countersurface. This process proved to be overly complicated and not responsive enough, therefore a PID controller was considered as an alternative. Even still, PID control was quite unnecessary and not stable enough with high noise, thus the final solution was to implement boolean

control with a moving window of the average force over each cycle. Other features of the LABVIEW control program for the tribometer include options to adjust the sliding distance and speed, ability to export two additional channels of data (i.e. voltage and current for tribocorrosion experiments), an emergency shut off, and live graphical viewing of the friction coefficient.

In developing the LABVIEW Visual Instrument (VI) that controls the tribometer, a number of issues were encountered along the way with regards to the electronics. First, synchronizing the position readout from the stepper motors and force/torque measurements from the transducer gave issues because there there is a frequency limit at which the microcontrollers can be pinged. If this value is exceeded, then the position readouts will lag behind and the internal buffer will continue to fill up, until which point the microcontrollers will no longer be able to report back to the computer. Although the microcontrollers individually control each motor, they all connect to a central USB (Universal Serial Bus) hub, and so if the position of two microcontrollers is pinged simultaneously, then the maximum frequency that they can be pinged will roughly be halved. A second issue that was encountered was aborting the LABVIEW program would improperly stop the system such that the microcontrollers would be left in a hanging state and could not further receive commands until power was shut off. Consequently, an emergency stop button for the front panel had to be implemented to safely stop the motors and re-enable the standalone program on the microcontrollers for manual control. A third and final issue found during system testing was the zeroing of the transducer which was addressed symptomatically. An indicator which shows all raw sensor readings was implemented to identify if the transducer wasn't properly zeroed and needed to be restarted.

3.5 Electrochemical Control of Sample

In order to incorporate wet testing for corrosion studies, a sample holder had to be designed that could properly seal the given samples which have a 2"$\times$1" footprint. A reservoir used to hold liquids was manufactured out of Delrin for its corrosion resistance and high strength (as opposed to acrylic which is quite brittle). To

produce a water-tight seal, the reservoir was clamped onto the sample with an O-ring that with applied pressure sits nearly flush with the flat surface of the sample – if the sampled is not flat however, then disposable butyl rubber sealant tape can be used in conjunction with the O-ring. The electrochemical cell is a three-electrode set up that makes use of a Ag/AgCl reference electrode which can be used in a wide range of pH (0 to 13.5) and temperature (0°C to 100°C), along with a platinum mesh counterelectrode chosen for its corrosion resistance and large surface area which provides a uniform electric field as depicted in Figure 3.5 and Figure 3.6. At room temperature and in 0.5 M NaCl, the potential with respect to the standard hydrogen electrode is approximately +0.25 V. The potentiostat used to control the potential of the aqueous environment relative to the sample or working electrode was a Princeton Applied Research model 273A potentiostat/galvanostat which can readily interface with our DAQ and output its voltage and current readings to two analogue channels as shown in Figure 3.7. While the potentiostat applies a potential the current is monitored between the counter and working electrodes, which in turn provides information regarding the rate of reaction.

The purpose of using such an apparatus for our experiments is to artificially induce an higher rate of corrosion. By doing so, the duration of tests can be shorter allowing for more trials to be performed and the observed effects of corrosion and material degradation are more prominent within the allotted time span of each experiment, both of which are beneficial. Normally in the field the environment surrounding a steel pipe may be at a given potential which would enhance corrosion, thus the electrochemical cell is supposed to impose similar and more consistent conditions which can be monitored in a laboratory setting. Going back to Equation (2.8), through the use of a potentiostat we can monitor the current flowing through the metal and determine the corrosion rate throughout our tribocorrosion experiments.

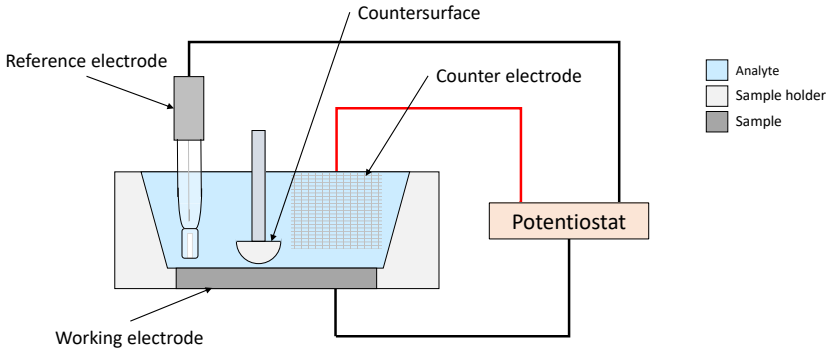

Figure 3.5: Three-electrode electrochemical cell schematic.

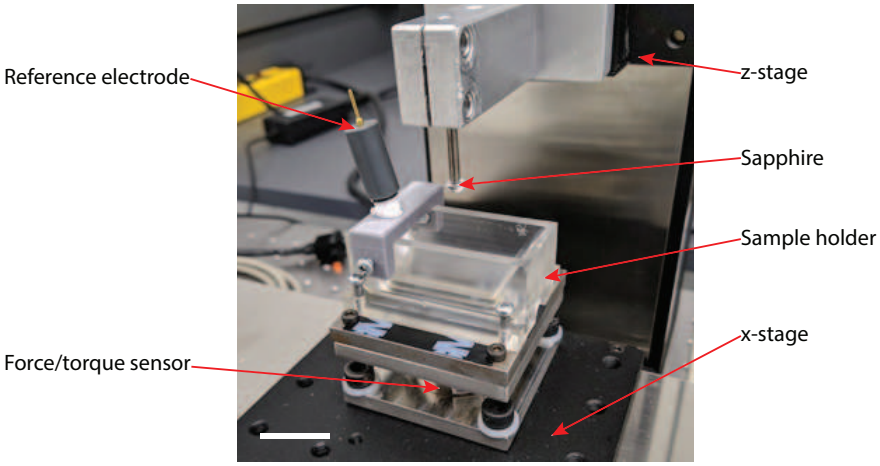

Figure 3.6: Close-up view of the actual sample holder. The white line in the bottom-left is 25 mm in length.

Figure 3.7: Princeton Applied Research model 273A potentiostat/galvanostat front panel [66].

Chapter 4

Experimental Procedures

This section describes the various types of experiments that generated the results contained within this thesis, as well as the manufacturing and preparation of samples that was conducted in advance of the experiments. This entails sample naming convention, dry sliding experiments, tribocorrosion experiments, potentiodynamic scans, optical profilometry, Scanning Electron Microscopy (SEM), and hardness testing. Within these procedures a number of standards are brought up from the American Society for Testing and Materials (ASTM) and International Organization for Standardization (ISO).

4.1 Samples

This thesis primarily involved the testing of steel samples under various environments. Table 4.1 describes the samples measured and the designations that will be used in subsequent sections of the thesis. In addition to boronizing, some coatings have been applied on top of samples for different effects. Flat steel samples were made from cold rolled bars cut to length with approximate dimensions $2" \times 1" \times \frac{1}{4}"$ with an approximately 4 mm diameter hole drilled at one end of the sample. This hole allowed for samples to be fixed rigidly to the force sensor in the plane of motion during testing, as well as allowing for easy sample removal/exchange

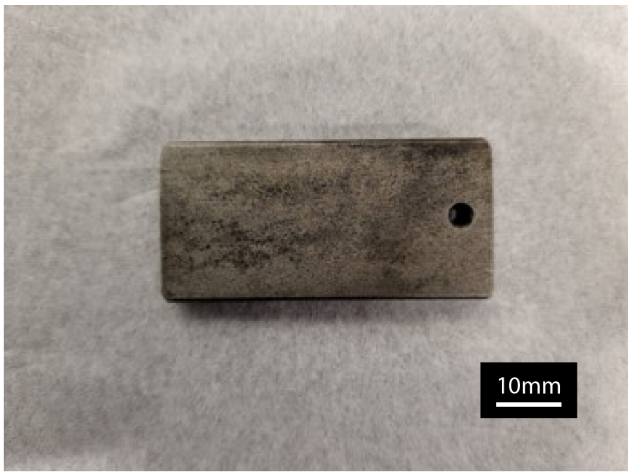

Figure 4.1: Photograph of a steel sample having dimensions of 2"$\times$1"$\times\frac{1}{4}$" with an approximately 4 mm diameter hole drilled near the right side of the sample allowing it to be fixed to the tribometer stage.

without disturbing the surface after experiments, such that surface characterization could be accomplished. An example steel sample is provided in Figure 4.1. In addition to the flat steel samples, steel pipe segments were also tested, the results of which are presented in Chapter 6. A straight pipe was cut length-wise into segments to match the same 2"$\times$1" footprint as all other samples. The curvature of the sample at the edges was ground flat to ensure that the liquid cell could make intimate contact with the samples, ensuring that the corrosive solution could not leak out during experiments.

Flat steel samples were polished with successively finer grit sand paper to achieve a mirror finish on surfaces prior to boronization processes. For pipe section tribological testing, no polishing was performed. Polishing was realized by grinding the sample with a 180 grit SiC paper in order to grind away mill-scale, and moving to progressively finer grits up to 1200 grit. Following polishing, the RMS roughness was measured to be 4.72 nm over a 10μm$\times$10μm area measured using the Scanning Probe Microscopy (SPM) imaging feature on our Bruker Hysitron TI Premier nanoindenter. This low roughness was important for ensuring a good contact between the 6 mm sapphire hemisphere counter surface and the sample, thus allowing for consistent and repeatable measurements between samples. Furthermore, the low roughness of the samples made subsequent measurement of the surface topography of the worn areas of the sample, used for determination of wear coefficients, more accurate.

Table 4.1: Sample labels and associated descriptions of the sample used in this thesis.

Label	Description
CS	AISI 1018 carbon steel sample containing 0.18 wt% carbon
316SS	316L stainless steel
B1	AISI 1018 carbon steel that has been boronized and also undergone immersion in hexagonal boron nitride suspension and low-temperature consolidation to produce a top BN-1 layer coating. The resultant steel has a total case depth of 0.006" and a coating thickness of approximately 5 μm to 10 μm.
B2	AISI 1018 carbon steel that has been boronized and also undergone immersion in hexagonal boron nitride suspension and low-temperature consolidation to produce a top BN-2 layer coating. The resultant steel has a total case depth of 0.006" and a coating thickness of approximately 5 μm to 10 μm.
B3	AISI 1018 carbon steel that has been boronized and also undergone immersion in hexagonal boron nitride suspension and low-temperature consolidation to produce a top BN-3 layer coating. The resultant steel has a total case depth of 0.006" and a coating thickness of < 1 μm.
BB	AISI 1018 carbon steel that has been boronized and undergone an additional proprietary thermal diffusion process using boron powders to produce a boron-rich top layer consisting of hexagonal-turbostratic BN-based compounds [67]. The resultant steel has a total case depth of 0.006" and a coating thickness of approximately 20 μm to 30 μm.
BN	1018 carbon steel that has been boronized and undergone an additional nitridation process to produce a nitrogen-rich top layer. The resultant steel has a total case depth of 0.006" and a coating thickness of approximately 5 μm to 10 μm.
PS	AISI 4715 carbon steel cut from a straight section of pipe

4.2 Dry sliding

Prior to performing dry sliding tests, samples often had a sight tilt to their surface when mounted on the tribometer. Thus, samples were first flattened on one side to allow for proper mounting without any rocking. Samples were mounted to a steel plate with an end-milled surface using a cyanoacrylate glue that could easily be removed later with a solvent such as acetone, which in turn was connected to the force sensor mount with four screws. Prior to starting reciprocations, the samples were gently cleaned with acetone to remove surface contaminants, such as finger oils, and the transducer readings were zeroed by letting the system rest for 2 seconds (1000 samples at 500 Hz sampling rate). Once force readings were correctly zeroed, the 6 mm sapphire hemisphere stylus was slowly lowered and pressed against the surface of the sample until the desired nominal load of 6 N was reached (this yielded a contact pressure of approximately 1.5 GPa). Upon reaching 6 N, the x-stage would begin reciprocation for 1000 cycles at 25 mm/s sliding velocity. It was found that 1000 cycles were sufficient for achieving a steady state friction coefficient beyond the run-in period for the majority of the dry sliding tests. As mentioned previously, the motions of the linear actuators of the tribometer follow a trapezoidal velocity profile in order to reduce the wear and tear on the moving components due to sudden changes in inertia. This however also leads to undesirable transient effects at the turnaround, therefore only the middle 60% of each cycle was analysed. It is common procedure to use a cut-off such as this, so that these transient effects can be eliminated from the measured data. The friction coefficient for each cycle was then calculated by taking the average sliding force divided by the average normal force. Once the test was concluded, the counter surface was replaced to ensure that the geometry was consistent for the next test (as later shown in Chapter 5, there was evidence of material transfer to the counter surface).

4.3 Tribocorrosion

Tribocorrosion experiments are carried out in a similar manner as dry sliding experiments. However, in the tribocorrosion experiments the sample surface was immersed in an aqueous environment and a three-probe electrical potential setup allowed for the measurement of corrosive current flow during sliding. In our case, we chose 0.5 M NaCl solution as the analyte which is similar in anionic concentration to seawater (which has a Reference-Composition Salinity of 35.16504 g/kg [68]).

Countless other corrosion experiments use this as a reference concentration. Compared to dry sliding, the load was kept the same at 6 N, but the sliding velocity was reduced to 6 mm/s as to prevent sloshing of the bath and wear and tear on the tribometer's gearbox. By either varying the concentration of ions or varying the potential of the sample with respect to its environment, one can control the rate of corrosion [24]; the latter option being much more feasible in terms of having a greater range of control of the corrosion rate. In order to limit the amount of current coming off of the sample, the exposed surface area was controlled by covering most of the sample with a polyethylene-based corrosion protection tape; this is also important as it is desired to have the majority of the corrosion occur at the wear scar. Only a 0.75"$\times$0.25" area of the steel was exposed to the corrosive solution, while the rest was covered by the tape. The reason for restricting the exposed area served dual purposes: to limit the amount of galvanic current received by the potentiostat so as not to overload the equipment, and to also have a known surface area to be able to calculate the current density. It is pertinent for these experiments that only the samples corrode, thus any such metal surfaces in contact with either the sample or analyte must be electrically insulated; the metal plate below the sample was lined with polyethylene-based corrosion protection tape and the hardened high-carbon steel rod attached to the counter surface was painted with nitrocellulose-based lacquer.

The first tribocorrosion experiment that we carried out for each sample was done with no applied bias at the corrosion potential (E_{corr}). This was considered as our control. Since there was no passivation behaviour of the coated samples in the NaCl solution at this potential, sliding was carried out immediately after

pouring the solution into the electrochemical cell. For subsequent tests, the applied bias was stepped up by increments of +50 mV to enhance the corrosion rate of the sample; the potentiostat was set to hold the potential at a constant value for the duration of the sliding. As described in the next section (Section 4.4), scans were performed to find parameters of the linearised Bulter-Volmer equation and to also find potentials for tribocorrosion tests. From the potentiodynamic scans, overpotentials were chosen for the tribocorrosion tests, typically ranging between +0 mV to +300 mV above E_{corr} in increments of 50 mV. During these test, hydrogen gas production was monitored visually to ensure that gas bubbles were only produced at the counterelectrode and not in the vicinity of the wear scar, ensuring that the reduction half-reaction was mainly occurring at the counter electrode in the experiments.

4.4 Potentiodynamic polarization

Polarization curves were acquired prior to carrying out any tribocorrosion experiments for two purposes: to determine the parameters of the linearised Bulter-Volmer equation that dictates the corrosion rate, and to find suitable potentials to use later for tribocorrosion experiments. In the following tribocorrosion experiments, it was also of interest to measure the performance of carbon steel and the coating that yielded the lowest friction or wear coefficient, and compare them with those acquired in dry sliding experiments described in Section 4.2.

As shown previously in Figure 3.5, the three-electrode electrochemical cell uses a Ag/AgCl reference electrode along with a platinum mesh which serves as the counter electrode. Samples were held in our custom designed electrochemical cell and their exposed surface area limited to a 0.75”$\times$0.25” area using polyethylene-based corrosion protection tape, the same as described in Section 4.3. Prior to conducting anodic and cathodic polarization tests, samples were left to passivate in the 0.5 M NaCl solution for 10 minutes. In accordance with ASTM G59 - 97, a scan rate of 0.1667 mV/s was selected for both anodic and cathodic scans [69]. First, a rough approximatation of the corrosion potential was measured using a hand-held

voltmeter. Anodic scans were conducted by starting just below the estimated corrosion potential and then gradually increasing the applied potential between the sample and environment, while cathodic scans were conducted by starting just above the estimated corrosion potential and then gradually decreasing the applied potential. Anodic polarization would enhance corrosion at the working electrode or sample, whereas cathodic polarization would merely promote the dissociation of water at the counter electrode. Measuring the current coming off of the sample with a known surface area exposed to the aqueous environment, a Tafel plot is then generated by plotting the logarithm of current density versus the potential of the sample with respect to the reference electrode. Furthermore, by applying a linear fit to the anodic and cathodic polarization curves each, the corrosion potential can be determined more accurately from the intersection of the two lines and the corrosion rate can be calculated if the average valency of the corrosion reaction is known [24].

4.5 Optical profilometry

After conducting friction testing, optical profilometry was employed in order to determine the amount of material removed due to sliding. A Zeta-20 optical profiler was used to measure the roughness of the surface of the sample. The Zeta-20 measures surface topography on the basis of white light interferometry. This is accomplished by making use of the wave superposition principle. Light reflected from the surface of the sample is split by a prism, which is then recombined at the photodetector to form an interference pattern based on the difference in phase (as shown in figure Figure 4.3), after which specialized software is then used to convert the interference pattern into the peaks and valleys that make up the surface of the sample [70]. In our case, multiple raster images of the wear scar are taken and then stitched together to then be analysed in MATLAB. Analysis involves identifying the boundaries of the wear scar, determining the average height of a mask applied outside of the wear scar region, flattening the profile using least squares regression, and then finally numerically integrating to obtain the positive wear, negative wear, and the difference between the two which is the wear volume used in the Archard wear equation.

Figure 4.2: Zeta-20 optical profilometer [71].

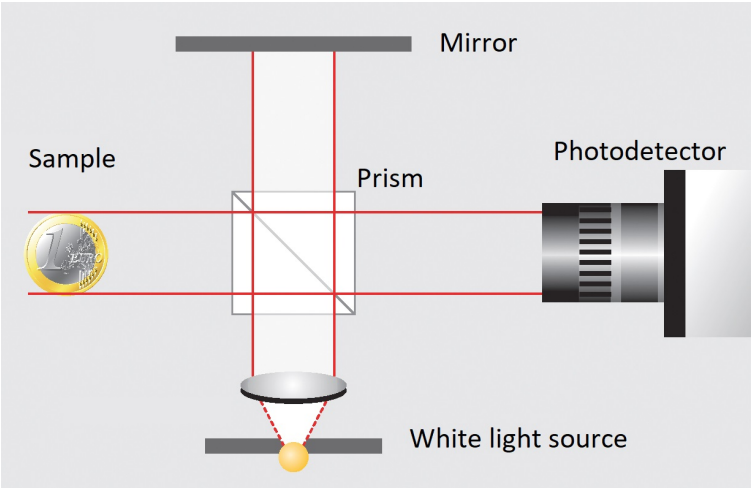

Figure 4.3: Schematic of white light interferometer [70].

4.6 Scanning Electron Microscopy (SEM)

SEM is a way of producing images by scanning the surface of an object using a focused beam of electrons that then interact with the atoms of the material, either providing information about the topography and/or the elemental composition. Depending on how electrons collide and interact – either elastically or inelastically – different information can be derived from the production of secondary electrons, back-scattered electrons, or even X-ray emissions. Although we would like to identify certain regions of interest for further visual inspection by examining images produced by back-scattered electrons (referred to as BSE images), we would also like to know more about the composition of the tribofilms left over from simultaneous erosion and corrosion of the boron coatings, namely using Energy-Dispersive X-ray Spectroscopy (EDS). BSE images are produced by electrons that are reflected back out of the sample by elastic scattering interactions with the sample atoms; these fast-moving electrons briefly orbit the atom before being ejected without slowing down [72]. The basic principle behind EDS is that a core shell electron of the sample is given sufficient energy by an incoming high-energy electron that it is knocked out of the atom inelastically and becomes a secondary electron; in addition, due to the Auger effect, an Auger electron is also emitted. This results in a vacancy which is then filled by an outer electron, resulting in the emission of a quantized X-ray with energy equivalent to the difference in energy level between the two shells. A detector on the opposing side of the incident electron beam collects these X-rays and is able to measure their energy, thus allowing the characterization of the elements from which these X-rays were generated [72]. While this process is particularly good for detecting the presence and composition of heavy elements, it is significantly more difficult to detect the presence of lighter elements, such as hydrogen, boron, or carbon, which are interesting for the types of coatings examined in this thesis.

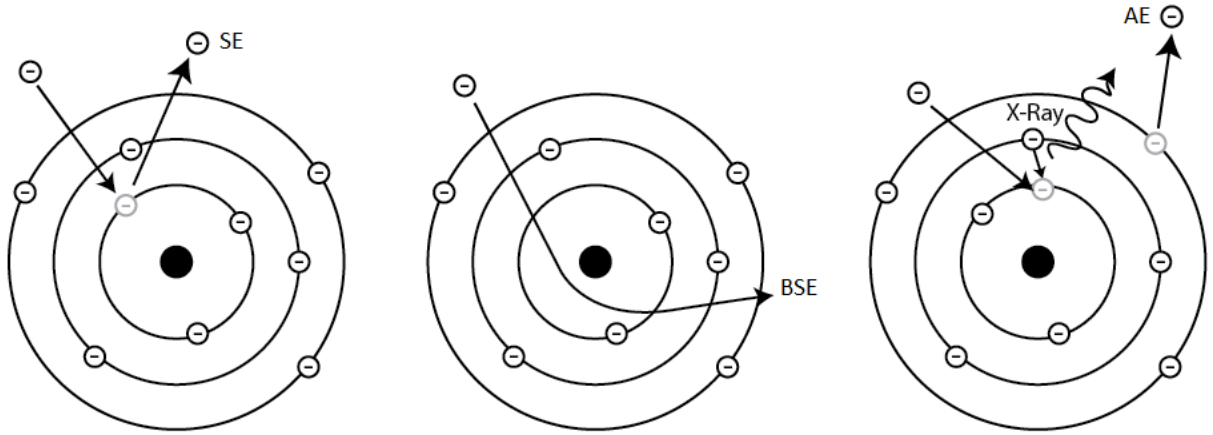

Figure 4.4: *From left to right.* Mechanisms of the various interactions of primary electrons with sample atoms to produce emissions of secondary electrons (SE), back-scattered electrons (BSE), and characteristic X-rays/Auger electrons (AE) [73].

4.7 Hardness testing

Both micro and nanoindentation were performed on polished cross-sections of the samples in order to determine the hardness of the coatings and their individual microconstituents (namely FeB and Fe_2B) in accordance with ASTM E384 - 17 standard [74]. Harndess testing, especially more-so when it comes down to nanohardness testing, is highly susceptible to environmental influences such as changes in temperature, humidity, acoustic noise, shocks, vibrations etc. [75]. Care must be taken to ensure that the set up is suitably isolated from shocks and vibrations particularly by means of passive isolation such as with a large granite block, optical table, or pendulumn suspension to provide mechanical damping. Also, it is important to note that performing hardness tests directly on the top surface of the samples is not feasible due to the high roughness, thus in order to evaluate the hardness of coatings, they must first be cross-sectioned, thoroughly polished, and then mounted in epoxy pucks for examination. Any variation in the flatness of the samples could result in inconsistent hardness values due to the nature of how hardness is calculated; the contact area of the indentation is based on known tip geometry under the assumption that the indent is performed on a plane-parrallel surface [76]. The hardness of the coating was used in conjunction with the Archard wear equation introduced previous in Section 2.1 is used to obtain the wear coefficient k. Without the hardness of

the material (i.e. for $H = 1$), we would otherwise obtain pseudo-wear coefficients, which are also important to consider as later explained in Chapter 5. For microindentation tests, we used a Buehler MicroMet 6000 machine with a Vickers tip and 200 g load mounted on a granite countertop. As for nanoindentation tests, we used a computer-controlled Bruker Hysitron TI Premier machine with a Berkovich tip which had a maximum load of 8000 μN for our specific set up. A comparison the the geometries of the two tips are shown in Figure 4.5. Although the size of the indenters appears the same in Figure 4.5, the Berkovich tip is actually not nearly as tall as the Vickers tip and is used with a much lower load, therefore produceing much smaller indents as presented in Figure 4.6. The hardness used in the Archard wear equation is the *indentation* hardness and uses the applied load over the *projected area* which corresponds to the area used for nanoindentation hardness tests. However, microindentation on the other hand uses the actual area of the tip in contact and thus a relationship is require to translate between Vickers hardness and indentation hardness. From ISO 14577-1 [77], we find that for the geometry of a Vickers tip

$$VH = \frac{2sin(136^{\circ}/2)P}{d^2} \tag{4.1}$$

which is in units of kgf/mm^2, and for nanoindentation which considers the hardness to based on the mean contact pressure

$$H = \frac{2P}{d^2} \tag{4.2}$$

which is in units of MPa. By substituting Equation (4.2) into Equation (4.1), then dividing the right-hand side by gravitational acceleration (9.81 m/s^2), we arrive at the final desired relationship shown below

$$VH = 0.0945H \tag{4.3}$$

Following ASTM E384 - 17, the standard specifies that the minimum thickness of the coating should be

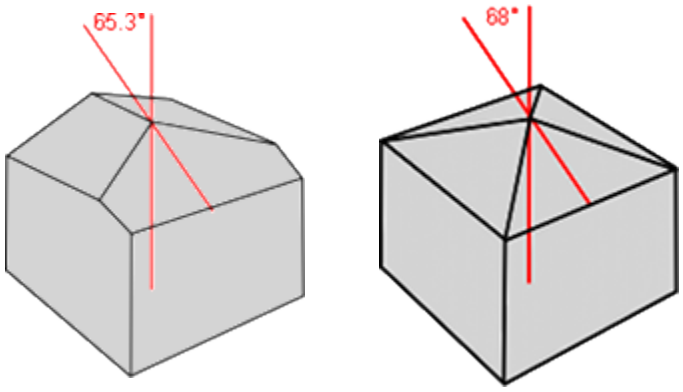

(a) (b)

Figure 4.5: *From left to right.* Indenter geometry of Berkovich and Vickers tips [78].

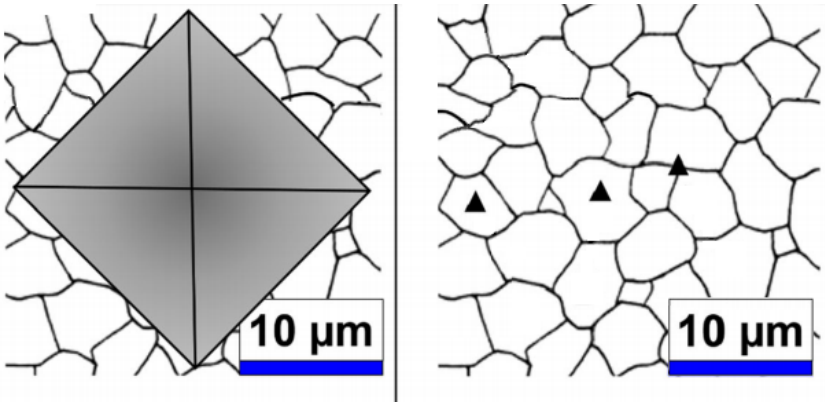

Figure 4.6: *From left to right.* Size comparison of the profiles of indents left behind by Berkovich and Vickers tips [79].

at least 10 times the depth of the indentation and that the depth of the indentation be at least 10 times the RMS roughness of the surface [74], which we confirmed for both microindentations and nanoindentations. With our instruments, indents could be viewed immediately after being performed – not only to measure their dimensions, but to also confirm that they were symmetrical in shape and confirm whether there were any resulting cracks which would invalidate an indentation. For our microindenter, indents could be viewed optically while for our nanoindenter, indents could be viewed using SPM imaging.

Chapter 5

Tribological Performance of Boronized Steel

This section describes the results from dry sliding friction experiments conducted on steel, stainless steel and boronized steel samples. The objective here was was to measure the friction coefficients acquired by sliding the 6 mm sapphire ball against these steel samples, as well as to determine the wear coefficients of these samples following the completion of the experiments. Following dry sliding experiments, the tribocorrosion performance of the boronized steel as a solution for erosion-corrosion of steel pipes is the evaluated against carbon steel and stainless steel samples.

5.1 Dry Sliding Experiments on Boronized Steel Samples

Figure 5.1 shows the friction coefficient versus cycle number acquired on all the provided boronized steel samples under dry sliding conditions (as per Table 4.1). These tests were performed with a 6 mm sapphire counter surface at 6 N applied load and 25 mm/s sliding velocity for 1000 cycles. The number of cycles performed was chosen based upon being able to reach steady value for the friction coefficient sufficiently

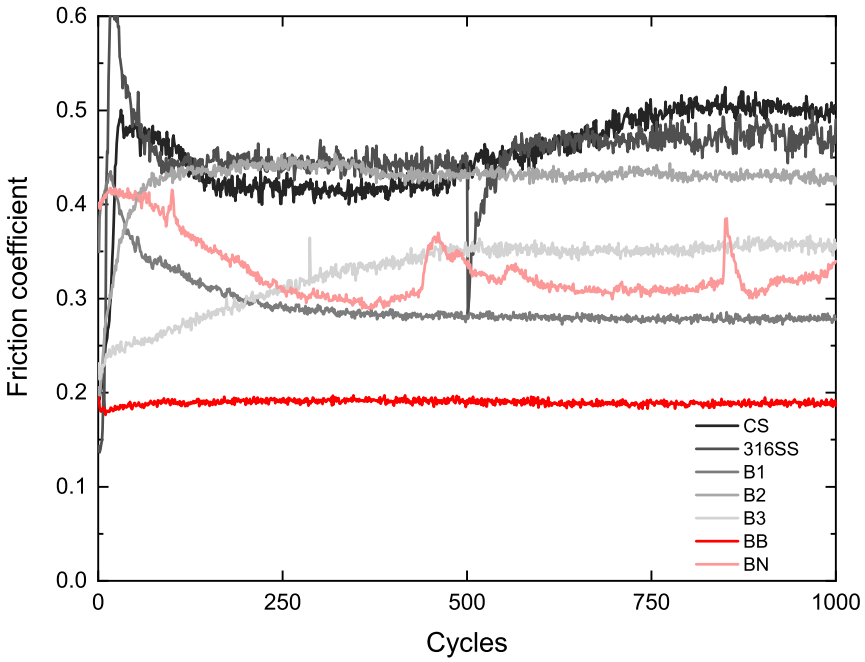

Figure 5.1: Friction coefficient versus cycle number of CS sample (black) and BB sample (red) acquired under dry sliding at 6 N load and 25 mm/s sliding velocity.

beyond the run-in period. This value showed the ability to reach a steady state friction coefficient for every test performed in these dry sliding experiments. Figure 5.1 also shows that the CS sample exhibited a friction coefficient of over twice that measured on the BB sample, showing a friction coefficient of $\mu = 0.386 \pm 0.002$ and $\mu = 0.189 \pm 0.003$, respectively, where the error is the standard deviation in the mean value calculated over cycle number 250 through 1000. Also, there was significantly more variance in the friction coefficient measured between 250 to 1000 cycles on CS sample compared to that measured on the BB sample. Additionally, the friction coefficient for the BB steel is nearly horizontal for the complete duration, indicating improved consistent tribological performance compared with the CS sample.

Figure 5.2 shows a bar graph of the steady state friction coefficient determined for seven steel samples: CS, 316 stainless steel (316SS), three different preparations for boronized steel (B1, B2, and B3), BB, and a nitrogen-rich boronized steel (BN). Figure 5.2 shows that the sample that had the highest friction coefficient was the 316SS sample. The 316SS sample yielded a friction coefficient of 0.46 ± 0.01, while all other thermal diffusion boron coated steels except for sample B2 performed marginally better than carbon steel. Finally,

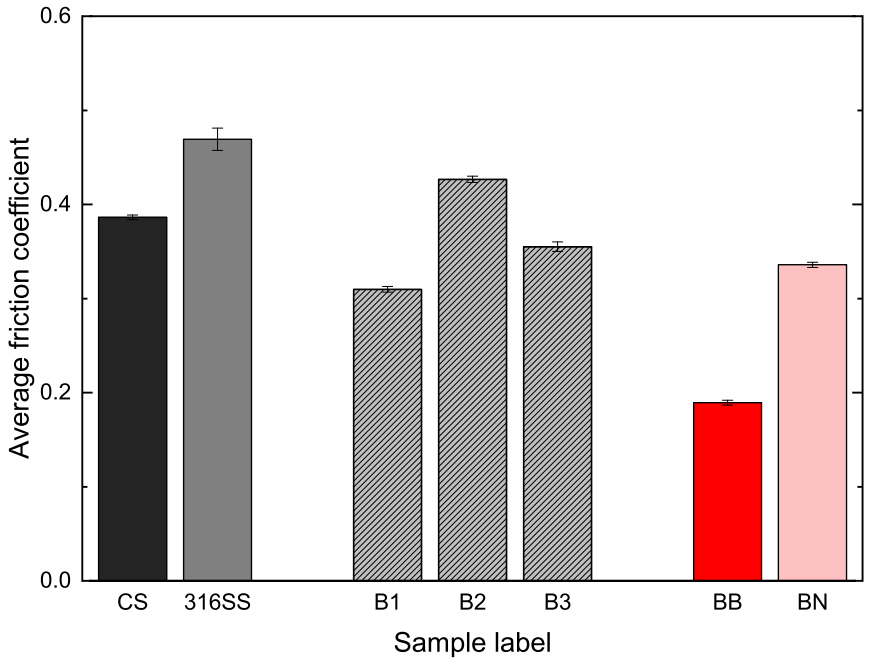

Figure 5.2: Average steady state friction coefficient of all samples acquired under dry sliding conditions using a 6 N applied load and 25 mm/s sliding velocity. The error bars indicate the standard deviation in the mean value of the average friction coefficient, determined from cycles number 250 through 1000.

the BB sample again performed the best, in terms of friction coefficients, compared with the other boronized steel samples. The BN sample showed that an enhancement of nitrogen at the surface did not lead to a significant improvement of the friction coefficient, compared with the CS sample.

In addition to the dry sliding tests that were performed on the seven steel samples above, a study on friction coefficient as a function of load dependency was performed for both CS and BB. Figure 5.3 shows the friction coefficient of CS and BB samples for various applied loads of a 6 mm sapphire ball sliding across the surface at a velocity of 6 mm/s. The purpose of these tests is to show that the friction coefficient should remain indiscriminant of load – at least up until a certain point where there may be serious destruction of the surface or the coating attached to the substrate. These series of load dependency dry sliding experiments were carried out at 6 mm/s sliding velocity for a total of 1000 cycles each for loads of 10 N, 15 N, 20 N, and 25 N.

Following tribological testing, the surface topography of the wear scars and the area surrounding them

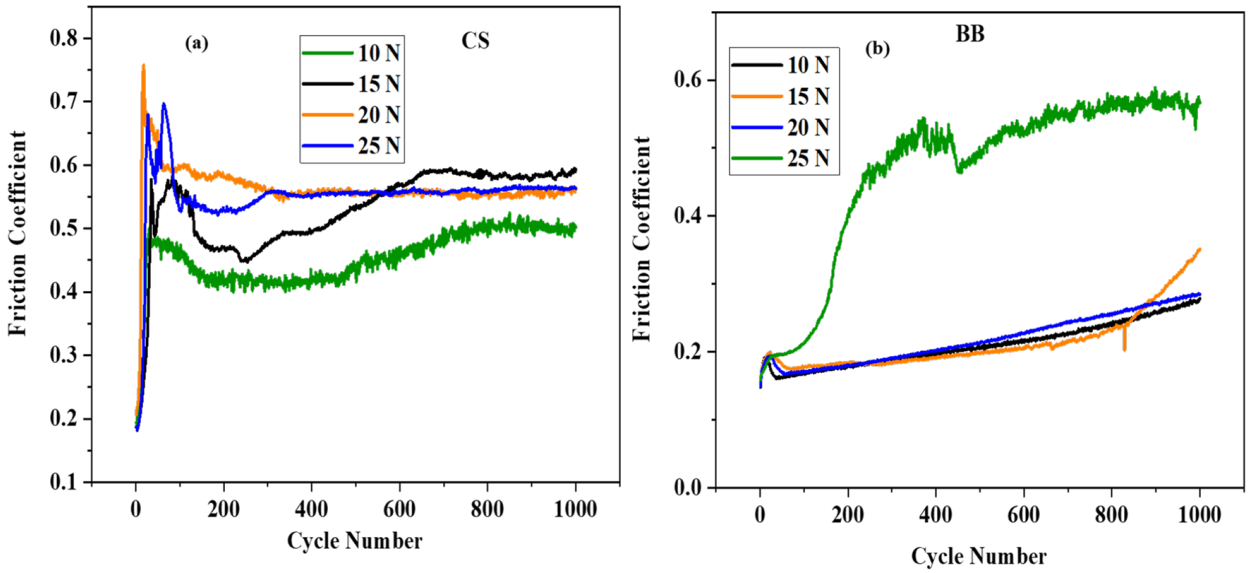

Figure 5.3: Friction coefficient versus cycle number of (a) CS sample and (b) BB sample acquired under dry sliding at 25 mm/s sliding velocity for applied various applied loads.

were captured using optical profilometry. Figure 5.4 (a) shows an optical image of the wear scar acquired with an optical profilometer. This technique also gives topographic information about the surface, in particular, allowing for the length and depth of the wear scar to be determined. Figure 5.4 (b) shows a line profile of the surface topography acquired along the dashed line in Figure 5.4 (a). Determination of these line profiles along the length of the wear scar allowed for the determination of the volume of material removed during the testing. To calculate the volume, the average surface topography with a 0 deg slope was calculated from outside the regions marked with the red 'x' in Figure 5.4 (b), and set to 0 μm height, as we observed almost no pile-up on the edges of the wear scars in the samples we tested. The worn area was then determined through a sum of the worn depth multiplied by the distance between the two red x's in Figure 5.4 (b). A subsequent summation of the same calculation for line profiles acquired along the length of the wear scar allowed for the determination of the worn volume. This information in combination with Equation (2.2) and the experimental parameters used during friction testing were used to determine pseudo-wear coefficients (essentially non-normalized in terms of H the hardness of the sample which is given a value of 1). Since the samples are macroscopically roughly made of the same material, other than 316SS, elimination of the

hardness value does not impact the comparison of the pseudo-wear coefficient between samples.

Figure 5.5 shows the variation in pseudo-wear coefficients for the different samples tested previously. Improved wear performance, or less material worn during tribological testing, appears in Figure 5.5 as a lower value of the pseudo-wear coefficient. In this case, the BN sample showed the worst performance compared with the rest of the samples. 316SS showed a similar poor wear performance, compared with the CS and boronized steel samples. The BB steel showed the best wear performance of all of the alloys tested in this series of dry sliding experiments. For this wear analysis of the steel samples shown in Figure 5.5, we have assumed that all wear was localized to the steel samples. However, given the high hardness of the samples in relation to the sapphire counter surface, wear of the hemisphere counter surface is likely. Figure 5.6 shows an optical image of the worn surface of the sapphire balls. The resolution of the optical profilometer paired with the high optical transparency of the sapphire balls was insufficient to acquire a topographic image to determine the quantity of the counter surface worn. However, optical images in Figure 5.6 did reveal that there was significant material transfer from the steel substrate (in this case for 316L stainless steel). Despite this observation, the fact that the counter surface was replaced for each test allows for wear performance of the steel samples to be directly evaluated by the Archard analysis performed in Figure 5.5 as the geometry of the counter surface should remain relatively consistent throughout the tests. Out of all the tests, those that exhibited the least amount of material transfer to the sapphires were the CS and BB samples. However, for the BB samples there were other small marks left behind on the counter surface indicating a slight change in the geometry.

5.2 Tribocorrosion Performance of Boronized Steels

Following the evaluation of the tribological performance of the boronized steels under dry sliding conditions, tribocorrosion experiments of the best performing samples from Section 5.1 were conducted. In these experiments, a three electrode electrochemical setup was used (as described in Section 4.3). In these

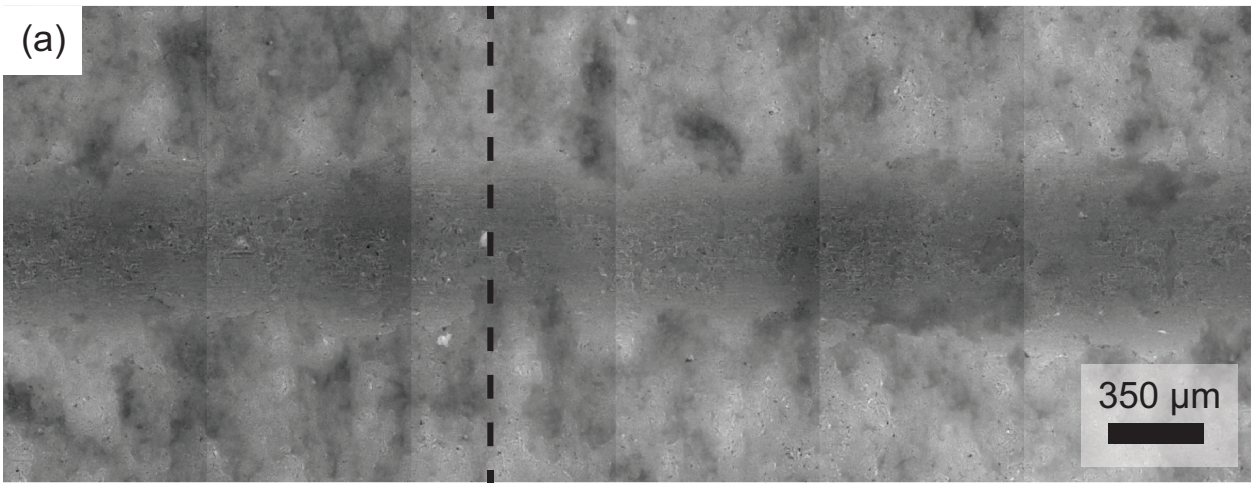

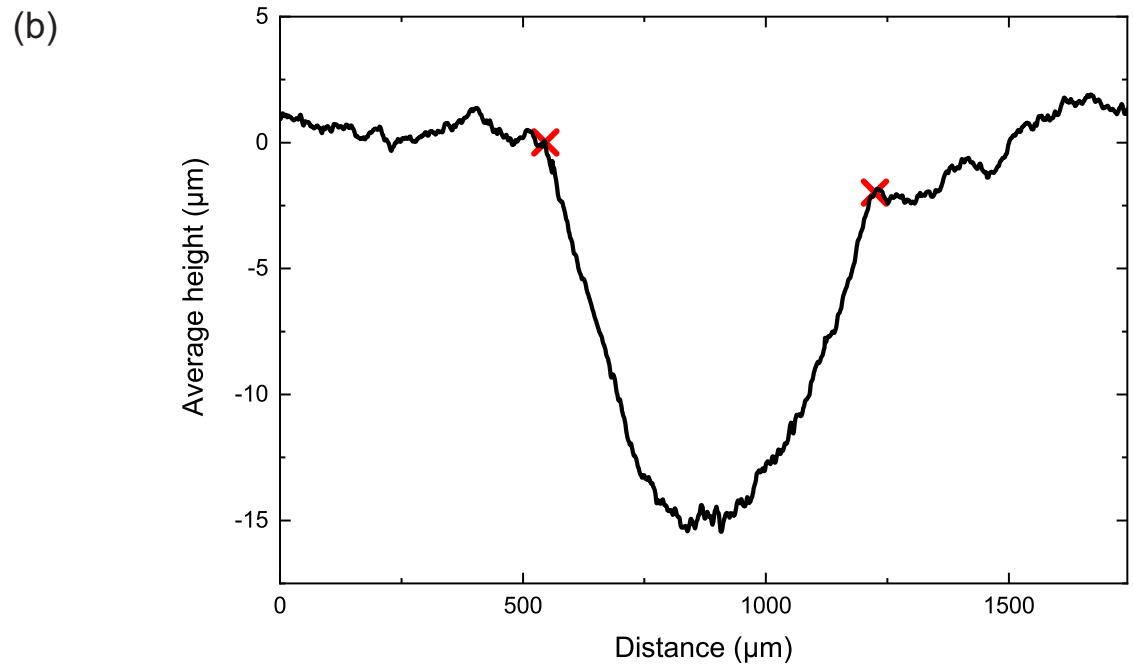

Figure 5.4: (a) Optical image of a wear scar produced in the B3 sample. (b) Profile of the wear scar acquired in (a) along the dashed line, indicating the depth of the scratch.

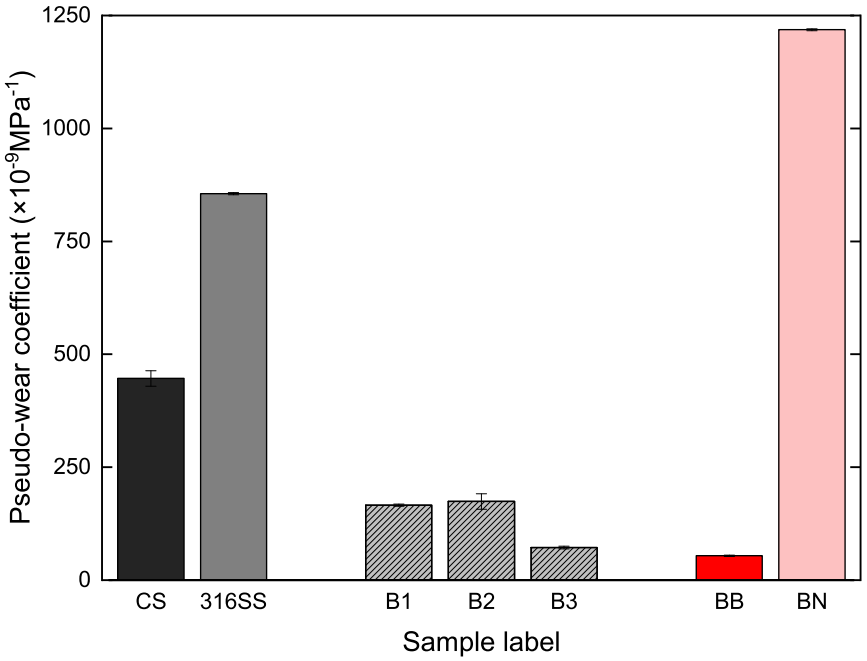

Figure 5.5: Pseudo-wear coefficients for dry sliding at 6 N load, 25 mm/s sliding velocity.

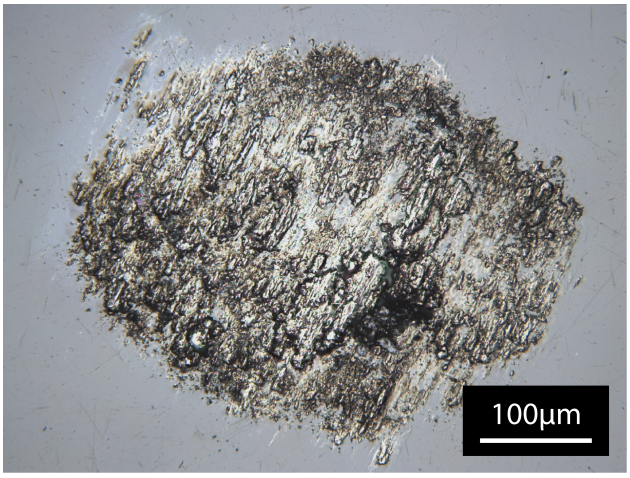

Figure 5.6: Optical image of 6 mm sapphire countersurface post-friction test. In this case the sample was a 316SS sample.

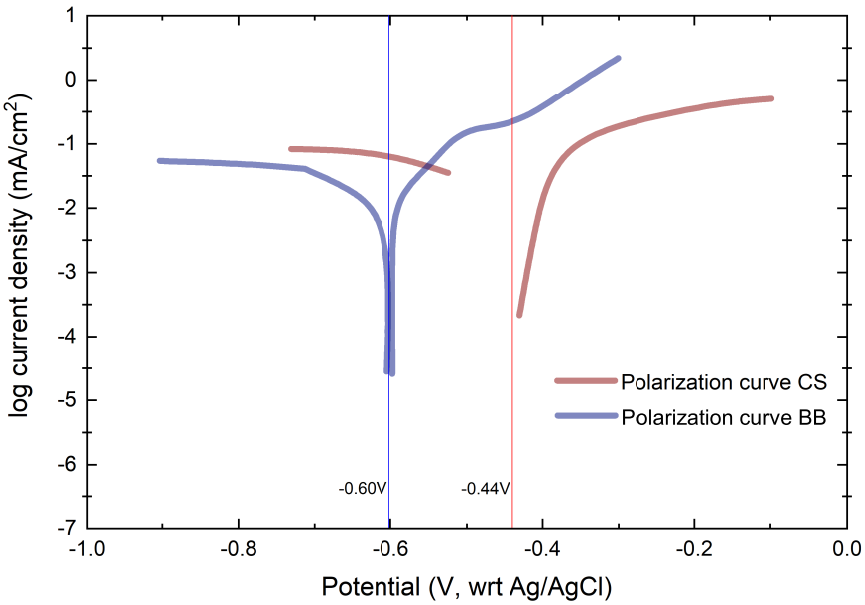

Figure 5.7: Polarization curve of carbon steel and boron-rich boronized steel in 0.5 M NaCl with linear fit applied to both the anodic and cathodic scan. All potentials are provided with respect to the Ag/AgCl reference electrode.

experiments, a potential was applied to the sample in reference to the counter electrode, which was also immersed in the analyte. The current was measured between the sample and a platinum mesh also inserted into the analyte. In these experiments, the counter surface and associated apparatus used to apply the load onto the sample with the counter surface are completely electrically insulating. However, before beginning tribocorrosion experiments, polarization curves of the samples, such as that shown in Figure 5.7, were generated to determine the corrosion potential and observe corrosion behaviour. The corrosion potential for the samples were determined from the intersection point of the linear regions anodic and cathodic of the polarization curves with the x-axis as per the Butler-Volmer equation (although we were not able to find the charge transfer coefficient α). In this case, the CS had a corrosion potential (E_{corr}) of -0.44 ± 0.01 V with respect to a Ag/AgCl electrode, while the BB sample had a corrosion potential of -0.60 ± 0.01 V with respect to a Ag/AgCl electrode. This value is then used in the subsequent graphs as the reference potential for tribocorrosion studies.

Figure 5.8 (c) shows the change in the friction performance between the sliding sapphire hemisphere

and the BB sample under various applied overpotentials meant to accelerate corrosion rates. Figure 5.8 (d) shows the average friction coefficient calculated for each overpotential from cycle number 1 through 250 in Figure 5.8 (a). Figure 5.8 (d) shows that as the overpotential was increased, the friction coefficient decreased slightly – this behaviour was reproducible for three trials at each overpotential.

5.3 Electron Microscopy Measurements on Boronized Steels

To gain better insight into the chemistry of the boronized steels, the impact of simultaneous corrosion and sliding on the chemistry at the surface, the overall microstructure of the steels examined, SEM imaging and chemical analysis of prepared surfaces were performed. First, in all SEM measurements, plane view sections of the wear scar were acquired on unaltered samples which were not cleaned or treated with any etchants following tribological and corrosive testing. This step was critical to ensure that the chemistry and structure of surfaces were conserved between testing and imaging.

Figure 5.9 (a) shows a SEM image acquired in the backscattered electron mode of a wear scar produced on a BB sample at an overpoential of $^{+}$0.30 V. The wear scar produced during tribological testing is highlighted with a red dashed oval, but also appears lighter in contrast than the unworn regions of the surface. Additionally, no significant pile-up was observed in Figure 5.9 (a), confirming the observation made in the optical white light images in Figure 5.4. Several microstructural features are apparent in Figure 5.9 (a), given the contrast evident in the image. Figure 5.9 (b) shows a higher magnification image of the worn BB surface inside the wear scar, a the location of the blue square in Figure 5.9 (a). Figure 5.9 (b) shows that the grains have a size on the order of microns.

In an effort to determine the origin of the contrast observed in Figure 5.9 (a) between the wear scar and the surrounding surface of the BB sample, energy dispersive X-ray spectroscopy (EDS) was performed on these two regions. Figure 5.10 (a) and (b) show the EDS spectra acquired both inside and outside the worn region of the sample, respectively. While EDS is not highly sensitive to light elements ($Z < 11$) [80], such

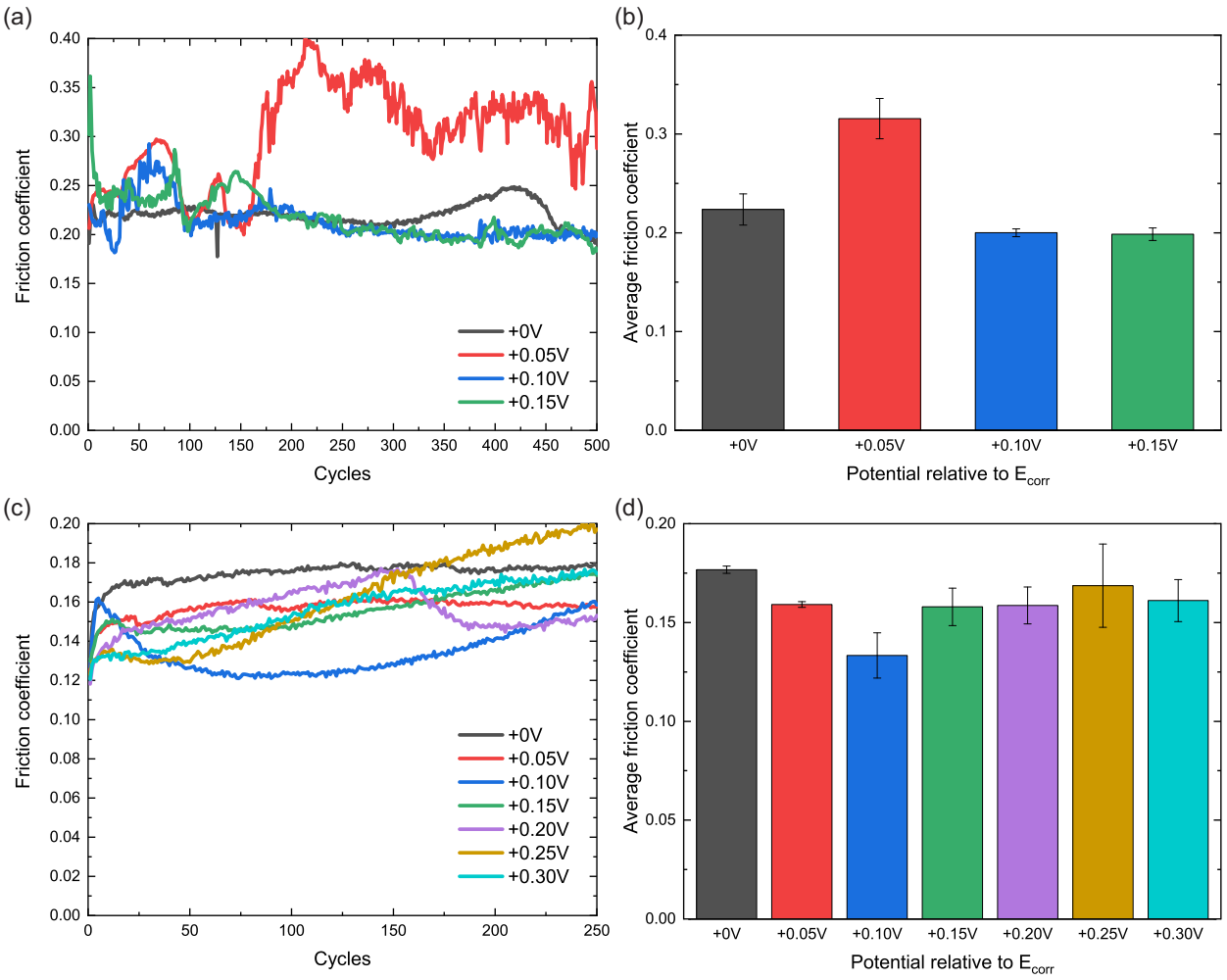

Figure 5.8: (a) Friction coefficient versus cycle number for various overpotentials and (b) average friction coefficient versus overpotential for CS sample. (c) Friction coefficient versus cycle number for various overpotentials and (d) average friction coefficient versus overpotential for the BB steel. In all cases, the samples were immersed in 0.5 M NaCl and a 10 N applied load and 6 mm/s sliding velocity were used. The error bars in (b) and (d) represent the standard deviation in the average value determined from (a) and (c), respectively, for cycles 1 through 250.

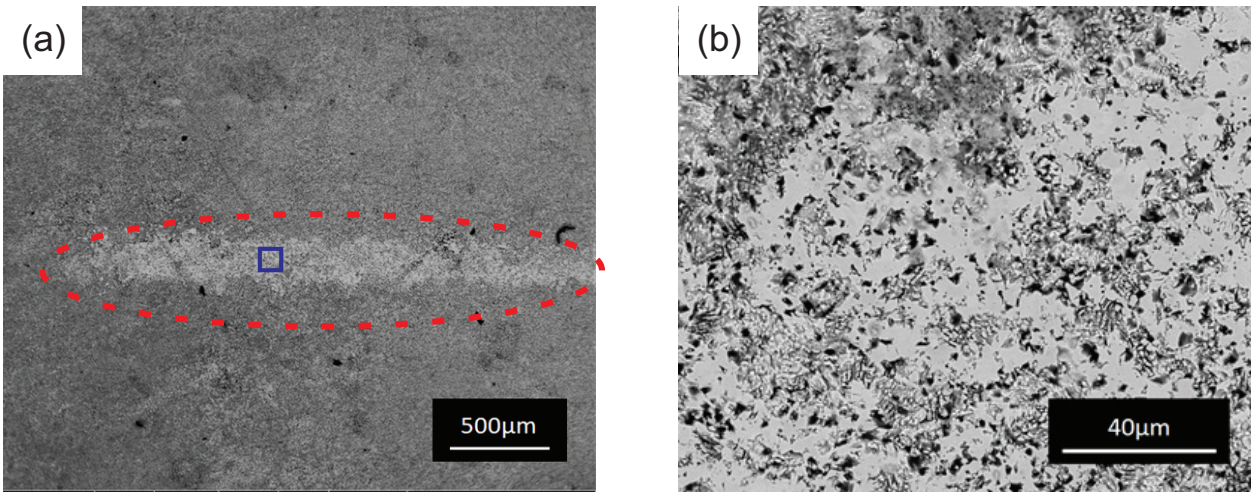

Figure 5.9: Plane view SEM images of a BB sample post tribological testing. (a) Backscattered electron mode image of wear scar (circled a red dashed line) of a BB sample tested at +0.30 V above E_{corr} in 0.5 M NaCl at 6 N load and 6 mm/s sliding velocity. (b) Higher magnification image acquired inside the wear scar on (a) in the region indicated by the blue square.

as boron, a marked change in the relative intensity of oxygen outside the wear track relative to the oxygen peak acquired inside the wear track is observed. Additionally, a significant decrease in the intensity of the iron peak with respect to oxygen peak is observed when comparing their intensities inside and outside the wear track. Thus, the brighter intensity inside the wear track is a result of the greater concentration of iron and lower concentration of oxygen, which appear brighter and darker in the backscattered electron mode because of their relative atomic contrast [81]. Beyond this information, no chemical information about the formation or absence of formation of a tribofilm, or film caused by the mechanical stresses and strains applied by the counter surface on the BB surface that has a different chemical make up than either the sample or the counter surface, can be interpreted from the EDS spectra.

5.4 Mechanical Property Measurements of Boronized Steels

To convert pseudo-wear coefficients, such as those expressed in Figure 5.5, to the dimensionless quantity expressed in Equation (2.2), the pseudo-wear coefficients must be normalized by the hardness of the sample. Following tribological testing, cross-sections of the CS, 316SS, and BB samples were prepared and polished

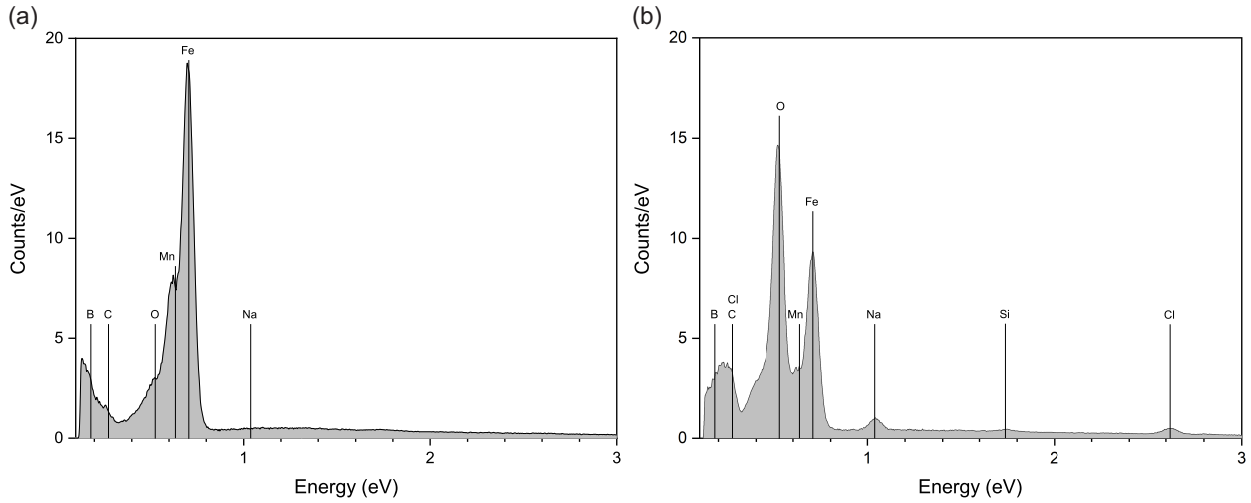

Figure 5.10: EDS spectra acquired (a) inside and (b) outside the wear scar. Characteristic peaks for various elements in the sample have been labelled in each case [82].

Table 5.1: Microindentation hardness data taken from cross sections of CS, 316SS, and the FeB/Fe_2B regions of the boronized steel. Indents were performed with a Vickers tip and 200 gf load.

Sample/layer	Vickers hardness (HV)		Indentation hardness (GPa)	
	Average	Std. Dev.	Average	Std. Dev.
AISI 1018 steel	130	10	1.3	0.1
316L stainless steel	230	10	2.4	0.1
FeB from boron-rich boronized steel	1500	200	16	2
Fe_2B from boron-rich boronized steel	400	200	5	2

to a mirror finish. Hardness measurements using a Vickers microhardness tester were acquired, and the data from these samples is summarized in Table 5.1. The results show that the 316SS was nearly 2 times harder than the CS sample, which is consistent with the published values for CS and 316SS [2, 83]. For producing a non-dimensional wear coefficient, the Vickers hardness values must be converted to SI units. This was realized by converting the maximum applied load applied by the indenter divided by the contact area between the indenter and the surface, as determined by the size of the impression left on the sample following the hardness measurement through Equation (4.2).

For the BB sample, two values of hardness were acquired through the cross section. As discussed previously in Section 2.2, the microstructure of BB steel due to the applied heat treatment process has two different regions with different chemical compositions and microstructure which can be seen in Figure 5.11. The FeB

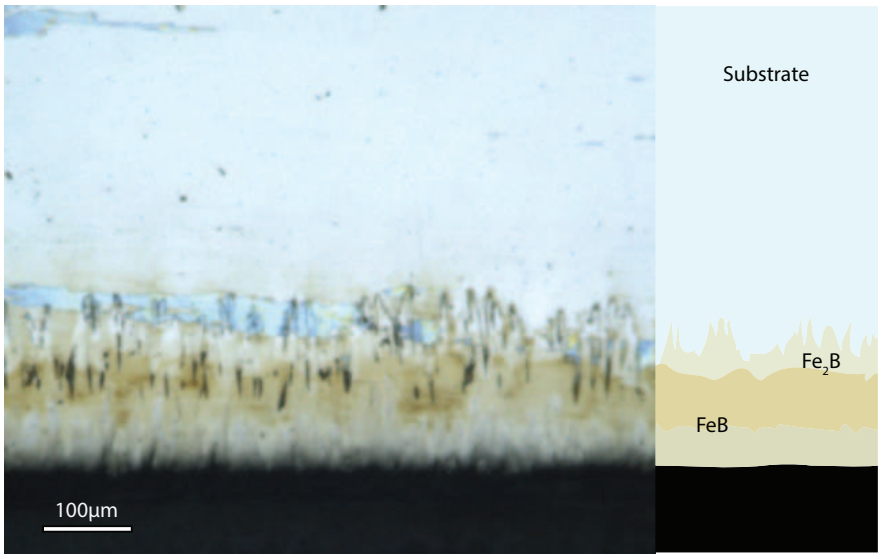

Figure 5.11: *On the left* an optical image of the microstructure of BB, and *on the right* a schematic describing the various layers.

region, which is closest to the surface of the steel, showed significantly enhanced hardness, nearly 4 times harder than the the Fe_2B region in between it and the substrate. The Fe_2B region in turn was approximately 3 times than the untreated substrate below it. In addition to the microhardness testing performed with a Vickers tip and 200 g load, nanoindentations were performed as to see if results were consistent, and to also reaffirm Equation (4.2). Nanoindentations taken using our computer-controlled Bruker Hysitron TI Premier machine with a Berkovich tip were performed in sets of 10 indents for each sample with a trapezoidal loading function (i.e. linearly increasing from zero load up to the maximum load, dwelling, then linearly decreasing back down to zero load). The maximum load for each test was 8000 μN, nearing the maximum capabilities of the machine in order to achieve as deep and as clearly visible indents as possible. In-situ images of each indent were taken using the scanning probe microscopy (SPM) imaging feature to confirm whether all indents were sufficiently deep enough in accordance with ASTM E384 - 17 standard, and only those that met the standard were kept. The purpose of this process was to check the invariance of hardness with respect to applied load for properly made indents. The results of the nanoindentations are summarized in Table 5.2 presented in SI units. Force versus indentation depth curves were also developed for all samples shown in Figure 5.12.

Once again, just as in the hardness tests performed with microindenter with a Vickers tip, the hardness

Table 5.2: Nanoindentation hardness data taken from cross sections of CS, 316SS, and the FeB/Fe_2B regions of the boronized steel. Indents were performed with a Berkovich tip maximum load of 8000 μN.

Sample/layer	Indentation hardness (GPa)	
	Average	Std. Dev.
AISI 1018 steel	5.37	0.41
316L stainless steel	8.67	0.61
FeB from boron-rich boronized steel	19.64	1.11
Fe_2B from boron-rich boronized steel	14.33	1.74

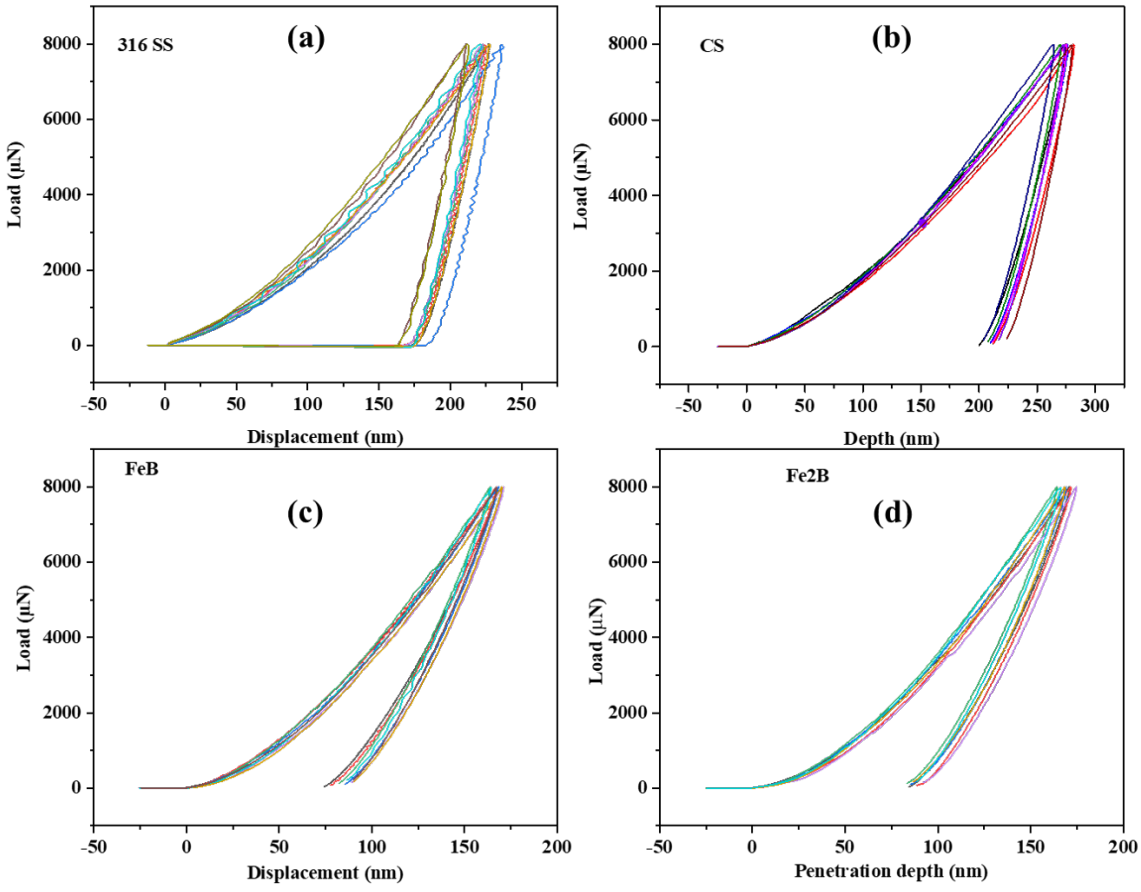

Figure 5.12: Nanoindentation force versus indentation depth curves for (a) AISI 1018 steel (b) 316L stainless steel (c) FeB from boron-rich boronized steel and (d) Fe_2B from boron-rich boronized steel. Indents were performed with a Berkovich tip maximum load of 8000 μN.

of the iron boride layers was drastically higher than the steel substrate. However, comparing the results side by side the indentation hardness values derived from the nanoindentations are significantly higher. The indentation hardness of the substrate from the nanoindentations was over 4 times greater than from the microindentations, and the indentation hardness of the stainless steel from the nanoindentations was about 3.6 times greater than from the microindentations. However, the indentation hardness of the FeB region which is critical to our studies of the boronized steels seemed to be in good alignement between the micro and nanoindentations.

5.5 Discussion

From the results of our dry sliding experiments, we found that the BB sample had the best performance with regards to both friction and wear. The friction coefficient of the BB sample in dry sliding with a 6 mm sapphire hemisphere was found to be 0.189 $\pm$0.003, which compared to that of the CS sample was 0.386 $\pm$0.002, providing a reduction in friction by a little over a half. Comparison with literature of these values is difficult resulting from the varying counter surfaces often studied for this material system. The most similar test performed in literature include sliding of a sapphire block against AISI 52100 steel gage block which yielded a friction coefficient of 0.13 to 0.14 [84], and a pin-on-disc test following ASTM G99 - 17 standard for boronized AISI 4140 gave a sliding friction coefficient of 0.2 to 0.4 [6]. Although there appears to be significant deviation between the experimental values and those just mentioned in literature, AISI 4010 and AISI 52100 are harder than AISI 1018 (AISI 4010 and AISI 52100 have a Vicker hardness of 207 HV and 848 HV respectively [85, 86]) and the surface roughness of these specimens are vastly different. Thus, the values should deviate slightly from what has been reported to our findings previously. From our dry sliding experiments, it was also noted that the friction coefficient over the 1000 cycles tested was also significantly steadier for the BB sample than the CS sample which indicates even wear and very little change in the surface morphology of the BB sample. All other types of boronized steel samples including B1, B2, B3, and BN

had marginal improvements in friction performance as compared to the CS sample, while the 316SS sample had a 20% increase in friction and quite a high friction run-in period as shown by the spike around cycles 1 through 100 in Figure 5.1. It should be noted that the friction coefficient for both the CS and 316SS samples were not nearly as steady as desired coming up on 1000 cycles of dry sliding, thus in retrospect it would possibly have been beneficial to continue tests up to 2000 cycles to achieve the same level of stability in the friction coefficient as exemplified by the other samples. The reason why a 6 N load was selected for many of these experiments is that this resulted in contact pressures of approximately 1 GPa to 2 GPa estimated using Hertzian contact mechanics [63, 64]. Looking back at Figure 5.2 (a), we can see that the friction coefficient for the 10 N applied load was lower than for the rest of the applied loads. Also, the friction coefficient did not remain completely stable for the entire duration of the 1000 cycles – it began to rise over the course of the experiment before somewhat leveling off. The case for 15 N load was similar in that there was a gradual increase in the friciton coefficient before leveling off, this time slightly higher than before. However, for the 20 N and 25 N load tests, the friction coefficient remained relatively constant throughout the experiment and quickly reached a steady state friction coefficient of 0.56. As for the BB sample, the results shown in Figure 5.2 (b) show that the friction coefficient was much more consistent between the 10 N, 15 N, and 20 N load tests, and also significantly lower by a factor of nearly a half. It was also observed that there were less perturbations in the friction coefficent than for the CS sample. But when the load was increased to 25 N, the friction coefficient drastically increased across the 1000 cycles, indicating that there was serious destruction of the coating occurring due to the high contact pressures, a behaviour which was not seen with the CS sample at this applied load.

Continuing with the results taken from dry sliding, the wear performance of BB looks promising as quantified by the pseudo wear coefficients. The pseudo wear coefficient of BB was $(0.54 \pm 0.02) \times 10^{-7}$ MPa^{-1} and for CS was $(4.47 \pm 0.02) \times 10^{-7}$ MPa^{-1}. BB exhibited an approximate reduction of a factor of 8 in terms of the pseudo wear coefficient compared with CS. Although it is almost always desirable to consider

non-dimensional or normalized values, pseudo-wear coefficients are more meaningful since only the material removal rate (usually stated in mm/hr or mm/yr) need be considered for most applications – the pseudo-wear coefficients presented here have been normalized in terms of load. Pseudo-wear coefficients are sometimes referred to as specific wear rates. Similar values close to 10^{-8} MPa were obtained for experiments involving steel samples in unlubricated condtitions [87]. An interesting result that came of the dry sliding test was the behaviour of the BN sample; although it had a relatively low coefficient of friction of 0.336 $\pm$0.003, the wear performance was strikingly poor, exhibiting a pseudo-wear coefficient of (1.22 $\pm$0.002)$\times 10^{-8}$ MPa^{-1} which is an increase of 2.7 times the wear of the CS sample and 1.4 times that of the 316SS sample. This poor wear performance makes BN an undesirable candidate for use in reciprocating sliding. As for the rest of the boronized steel samples B1, B2, and B3, they all demonstrated low wear less than half of that of the CS sample, but there was no strong correlation between the friction and wear coefficients to be seen.

Friction is closely correlated to adhesion or bond strength of a material whereas wear is more closely related with hardness [88]. Due to the high surface hardness of the coatings, which we measured with both our microindenter and nanoindenter, wear was greatly improved as supported in previous literature [5, 42, 48]. However, the indentation hardness values for the different samples acquired from the two methods differed by as much as 4 times. However, taking into consideration the size of the Vickers indenter, the microhardness measurements taken may be somewhat skewed given that indentor is close to the same scale as the thickness of the different coating layers. Thus, significant influence from the substrate in microhardness indents cannot be excluded. This dimensional challenge is why ASTM E384 - 17 specifies that the minimum thickness of the coating should be at least 10 times the depth of the indentation [74]. Both microhardness and nanohardness tests serve unique purposes: microhardness tests are more suitable for determining the average hardness across several grains since indentations cover a larger area, as opposed to nanoharndess tests which can more readily distinguish the hardness of individual phases, microconstituents, or thin coatings but results may be more heavily influenced by defects and crystal orientation [79]. Because of this, we would prefer to use the

indentation hardness values given by the nanohardness tests as the localized mechanical properties for these experiments as they are more relevant to the wear of the thin FeB layer itself. Factoring the hardness of the FeB layer of the BB sample provides another perspective on the wear of the coatings. If we use the hardness data from the nanoindentations, given that the hardness values extracted from these tests are more reliable given the fact that we have the complete force versus indentation depth curves, as well as more accurate indentation hardness for the Fe_2B region, the non-dimensionalised or real wear coefficients of CS and BB are $(2.40 \pm 0.65) \times 10^{-3}$ and $(1.05 \pm 0.21) \times 10^{-3}$ respectively.

For the tribocorrosion studies of the best performing sample from the dry sliding experiments conducted in Section 5.1, it was observed that the friction coefficient of the BB sample in 0.5 M NaCl decreased with artificially induced electrocorrosion as can be seen in Figure 5.8 (c) and (d). On the other hand, for the CS sample there is no apparent relationship between friction coefficient and enhanced electrocorrosion above E_{corr}. Experiments conducted at overpotentials of +0.10 V and +0.15 V yielded curves for friction coefficient versus cycles that were similar one another. For further experiments conducted at E_{corr}, only a slight increase in the friction coefficient was observed from 350 through 450 cycles. The only anomaly recorded from these series of experiments was for an overpotential of +0.05 V. At this potential, a very high coefficient of friction throughout the experiment was observed, as well as a high degree of fluctuation in the friction coefficient with the number of cycles. These observations were not seen at any higher overpotentials. These experiments were repeated twice, both showing similar trends in the experimental results. Without further experimentation, mechanism responsible for this variation in friction coefficient with varying potential on the BB sample cannot made. However, we can draw some hypothesis from our chemical characterization acquired by the EDS analysis. The EDS spectra showed a much higher oxygen peak outside the wear scar where there was the pileup of debris. This peak further dominated the iron peak for this same region. In comparison, the relative intensity of the oxygen peak in relation to the iron peak was substantially smaller inside the wear scar. It is well known that boron has a high affinity for oxygen and that borides have a tendency to form a

thin oxide film [89]. We propose that the reciprocating sliding leads to the continuous removal of the thin oxide film produced due to corrosion, which in turn promotes the development of a unique tribofilm that could be acting as a lubricant or an antiwelding surface to reduce the friction coefficient during sliding. This hypothesis of the wear of oxide films being a mechanism for reducing friction is supported by sources, but has yet to be proven [9,47,90,91]. The reason as to why CS does not exhibit the same behaviour as BB, for which tribocorrosion reduced the coefficient of friction, is likely that the development of iron oxides or rust merely roughens the surface leading to increased fluctuations in the coefficient of friction as seen in Figure 5.8 (a).

To elaborate on why such fluctuations seem to be present in the friction coefficient over time for all of the tests performed, as sliding occurs the wearing down of asperities and filling in of valleys changes the surfaces roughness, and the oxidation reactions serve to enhance the shaping of the surfaces under sliding. This alters not only the surface geometry, influencing the contact area and elastic interactions, which in turn affects the normal force and local shearing resistance of the contacts during sliding. This behaviour of fluctuations in friction coefficient during sliding due to the evolution of contacts has been observed in simulations [92]. This is especially pertinent to the conditions of our macroscale experiments which involve multi-asperity contact [93].

5.6 Summary

Reciprocating friction experiments were conducted under dry sliding and electrochemical conditions on several different steel samples. Dry sliding examination of boronized steels showed a general improvement in the friction and wear performance of the samples, compared with carbon steel or stainless steel, unless the boronized surface was doped with nitrogen. We also conclude that the BB sample exhibits significantly lower friction coefficient at nearly all loads for dry sliding until the contact pressure becomes too high such that serious destruction of the coating becomes a concern. Further, an excess concentration of boron in the boronized steel samples showed the best performance of all samples in terms of friction and wear. In

electrochemical tests in 0.5 M NaCl, a non-monotonic variation in the friction and wear performance of CS and BB steels were observed, with the BB steel still performing better than the CS in all experiments. Artificially induced corrosion of BB at various overpotentials showed a decrease in the coefficient of friction. Chemical analysis of the wear scars suggest that any oxides formed under the corrosive solution is removed by the sliding action of the tip against the steels.

Chapter 6

Erosion Corrosion of Steel Pipes Under Various Conditions

This chapter describes a second tribocorrosion project on steel substrates, similar to those discussed in Chapter 5. Rather than performing tribological experiments on steels that have undergone various boronizing processes, in this chapter the erosion-corrosion performance of real sections of pipes used in hydraulic fracturing are examined under ideal electrochemical conditions, as well as to emulate environments exposed to these steel pipes in a controlled manner. First, the friction and wear performance of the pipeline steel will be examined under water extracted from the actual site where hydraulic fracturing is performed. The analyte is called "High Total Dissolved Solids (TDS) water" and contains high salt content on the order of 200,000 ppm or greater along with sand and silt. Followed by the examination of the baseline performance of the steel under the high TDS water, friction reducers commonly used by CalFrac Well Services to improve the performance of their operations is evaluated. Finally, the impact of an oxygen scavenger, an additive that removes the dissolved oxygen in the water, on the two preceding studies is examined as one possible solution to mitigate erosion-corrosion in the steel pipe.

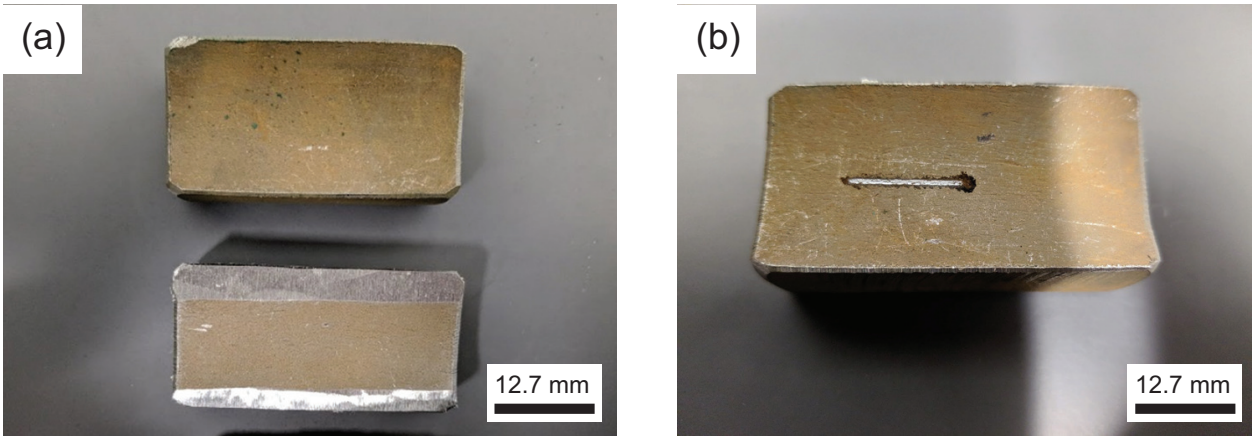

Figure 6.1: (a) *From top to bottom.* Pipe sample before and after grinding the top and bottom edges of the curved pipe section in order to allow fluid cell for tribometer to provide a water-tight seal. (b) Pipe sample after dry sliding test at 10 N load and 25 mm/s sliding velocity for 10,000 cycles.

6.1 Friction and Wear Performance of Steel Pipe Samples in High Total Dissolved Solids (TDS) Water

Figure 6.1 (a) shows an image of the sections cut from a pipeline used in hydraulic fracturing. This resulted in samples that were not flat, and rather had some curvature to them (in the vertical direction). The curvature of the sample prevented a water-tight seal to be formed through mechanically pressing the fluid cell against the sample. To form a water tight seal, the edges of the sample were ground to be flat as shown in the lower sample in Figure 6.1 (a). As can be seen in this image, most of the sample remains unaltered as a result of this grinding process. In all cases, the pipes were cut with a high-pressure water jet to the dimensions required, minimizing the possibility of microstructural changes to the material. The pipe samples were not modified in any further (no polishing was done) with exception to a gentle cleaning of the surface using acetone.

Following the grinding procedure, dry sliding experiments were conducted on the pipe sample to see if friction testing was viable for their curved geometry as all previous tests had been performed on flat samples. Figure 6.1 (b) shows an image of the same section of pipe after having performed a dry friction test. Here, it can be seen that the pipe is oriented such that sliding occurs along a line with zero curvature (i.e. following

the longitudinal direction of the straight pipe). In comparison to the steel samples tested previously, the the Vickers hardness is approximately 227 HV which is harder than the untreated carbon steel which is 130 HV [94]. This coupled with the high surface roughness as the pipe samples were left unpolished resulted in a significant decrease in the wear rate, which is why the cycle number was increased to 10,000 reciprocations. The increase also allowed for a significant wear scar to be produced, that can be optically identified.

6.2 Effect of Friction Reducers

The first solution to improving the erosion-corrosion behaviour of steel is to reduce the friction coefficient between the fluid and particles in the hydraulic fracturing fluids. The addition of friction reducers to the fracking fluids can thus reduce their negative impact on the erosion due to proppants on pipelines [13, 95]. Thus, the impact on friction between the sapphire counter surface and the steel pipeline in the presence of friction reduces was examined in the presence of high TDS solutions. More specifically, experiments were conducted with two commercial friction reducers: DynaRate 6524 and DWP 621. Both are polyacrylamide (PAM) based friction modifiers, but DWP 621 is an anionic water-soluble polymer whereas DynaRate 6524 is a cationic water-soluble polymer [96]. Figure 6.2 shows the variation of the friction coefficient with cycle number for the high TDS solution, as well as for the same solution with the addition of the two friction modifiers.

Figure 6.2 shows a baseline test was performed in high TDS water without any friction reducer at 10 N load and 6 mm/s sliding velocity for 10,000 cycles. After a brief run-in period of approximately 2500 cycles, the friction coefficient levelled out at an average of $\mu = 0.105 \pm 0.003$ taken over cycles 2500 through 10,000, with the error being the standard deviation in the mean calculated over this period. As seen in Figure 6.2, the friction coefficient remained relatively consistent once the run-in period was surpassed, as the friction coefficient remained nearly horizontal for the duration beyond run-in. In the next two tests, each friction reducer was added to the high TDS water at 3/1000 parts volume and thoroughly mixed. Figure 6.2 shows

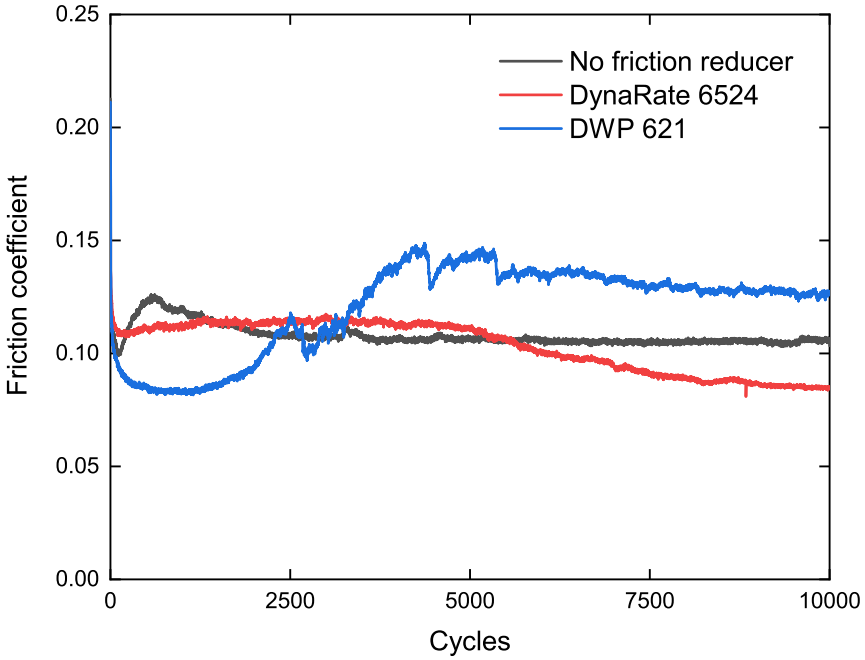

Figure 6.2: Friction coefficient versus cycle number of straight pipe in 0.5 M NaCl at 10 N load and 6 mm/s sliding velocity with various additives.

that for the test with DynaRate 6524, the friction coefficient began to decrease after approximately 5000 cycles but had a notably longer run-in period compared to the base TDS solution. The average friction coefficient for DynaRate 6524 taken over cycles 7500 through 10,000 was $\mu = 0.085 \pm 0.003$, a 20% reduction in friction as compared to without any friction reducer. On the other hand, Figure 6.2 shows that with DWP 621, the friction coefficient was initially lower than the TDS solution without any modifier, as well as the DynaRate 6524, but subsequently increased before plateauing out at $\mu = 0.127 \pm 0.004$ taken over cycles 5000 to 10,000. This value for the friction coefficient represents a 20% increase in the friction coefficient as compared to the TDS solution without any friction reducer. The friction coefficient with DWP 621 was also not as steady during the duration of the test. These tests were performed three times for each condition. Following friction measurements, the impact of the friction reducer on the wear coefficient was examined. Figure 6.3 summarizes the difference in the pseudo-wear coefficients between the high TDS solution and the same solution with the DynaRate 6524 and DWP 621 friction reducers added. When it came down to the pseudo-wear coefficient, images of the surface topography were acquired and analyzed in the same manner as in Chapter 5. Without

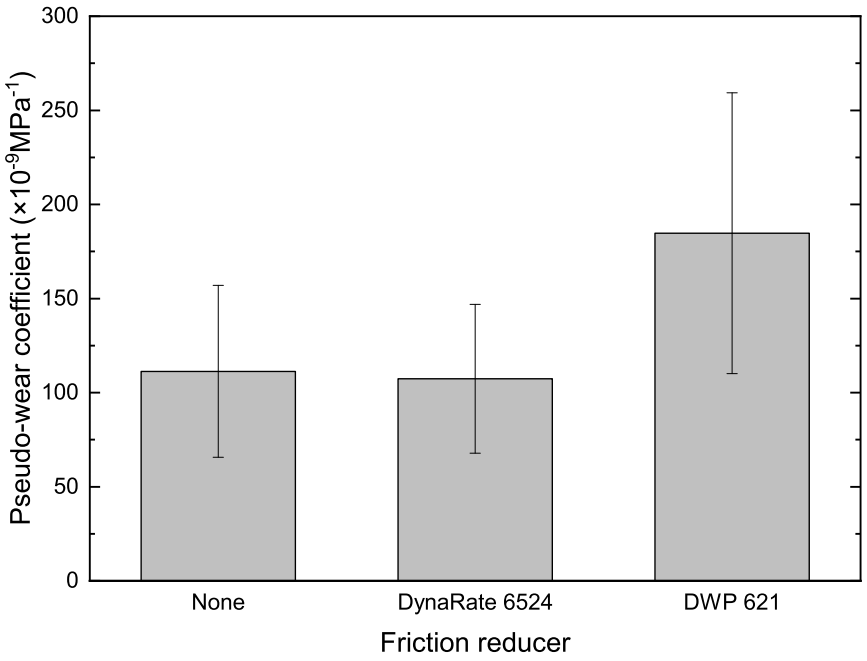

Figure 6.3: Pseudo-wear coefficients for straight pipe in high TDS water at 10 N load and 6 mm/s sliding velocity for various additives.

friction reducer $k = 1.11\times10^{-7} \pm 0.46\times10^{-7}$, with DynaRate 6524 the $k = 1.07\times10^{-7} \pm 0.40\times10^{-7}$, and with DWP 621 $k = 1.85\times10^{-7} \pm 0.75\times10^{-7}$. The wear rates for tests without friction reduce and DynaRate 6524, the pseudo wear coefficients were identical within the error of the measurement, while the test with DWP 621 showed a markedly higher pseudo-wear coefficient.

Figure 6.4 shows optical images and associated surface topographies from the three experiments performed in Figure 6.2. Optical images and line profiles of the wear scars for are shown together side by side with the profile data, where Figure 6.4 (a) was the profile acquired with no friction reducer, Figure 6.4 (b) with DynaRate 6524 reducer, and Figure 6.4 (c) with DWP621 friction reducer. Correlation of the results from Figure 6.3 and Figure 6.2 shows that DWP 621 yielded the poorest results for both friction and wear performance. Thus, this friction reducer was no longer considered viable for use in future tests and only DynaRate 6524 was investigated further.

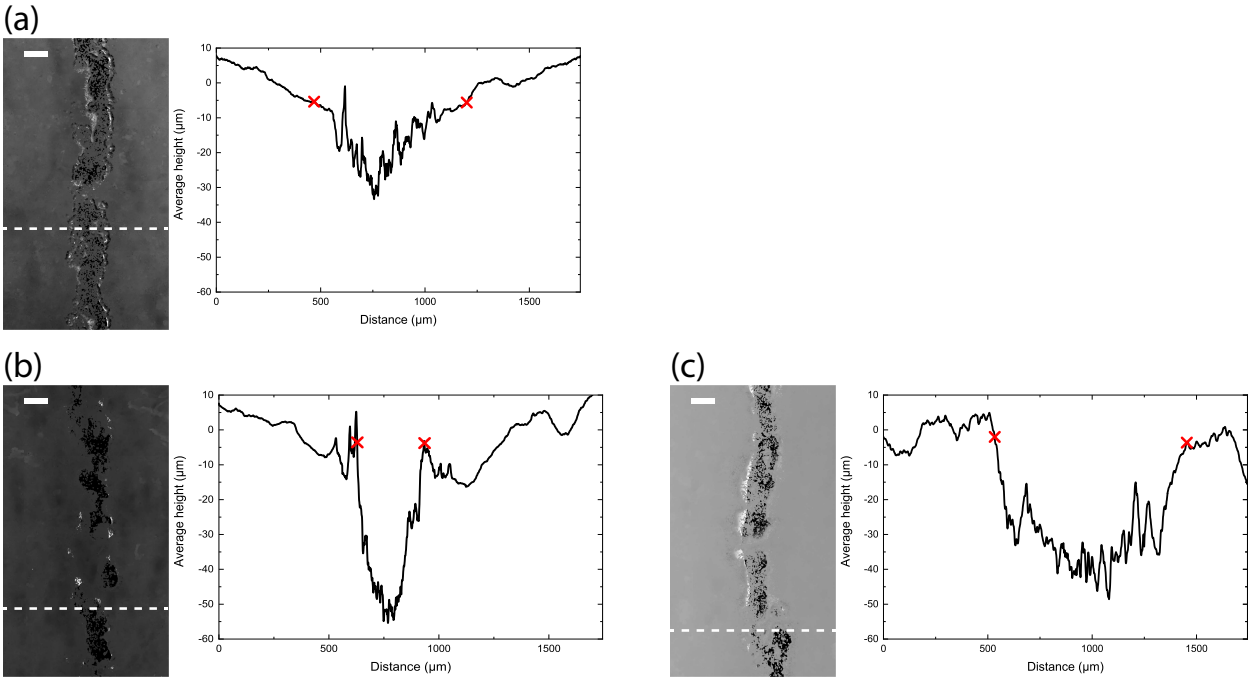

Figure 6.4: Optical image of wear scars along with profile of the wear scars used to acquire the pseudo-wear coefficients of straight pipe in 0.5 M NaCl at 10 N load and 6 mm/s sliding velocity for various additives: (a) no friction reduce, (b) DynaRate 6524, and (c) DWP 621. The white line in the top-left of each optical image is 250 μm in length.

6.3 Electrochemical Effects on Friction Performance of Steel Pipe Samples

The result of Section 6.2 was that DynaRate 6524 performed significantly better than the TDS solution without additive or with the DWP 621 additive. Thus, the focus of all future tests of erosion-corrosion performance only used DynaRate 6524 reducer. Figure 6.6 The following tribocorrosion tests were conducted once again in high TDS water and with DynaRate 6524 added at 3/1000 parts volume at 10 N load and 6 mm/s sliding velocity, for arbitrarily chosen overpotentials. Figure 6.6 shows the friction coefficient versus cycle number under the effect of no applied potential, and overpotenials of +10 V, and +100 V. With increasing overpotentials, friction was observed to increase making the DynaRate 6524 friction reducer less effective. In particular for +100 mV overpotential an extreme fluctuation in friction coefficient was initially observed from cycle 1 through 2500 followed by the friction steadily increasing thereafter through to cycle 5000. For

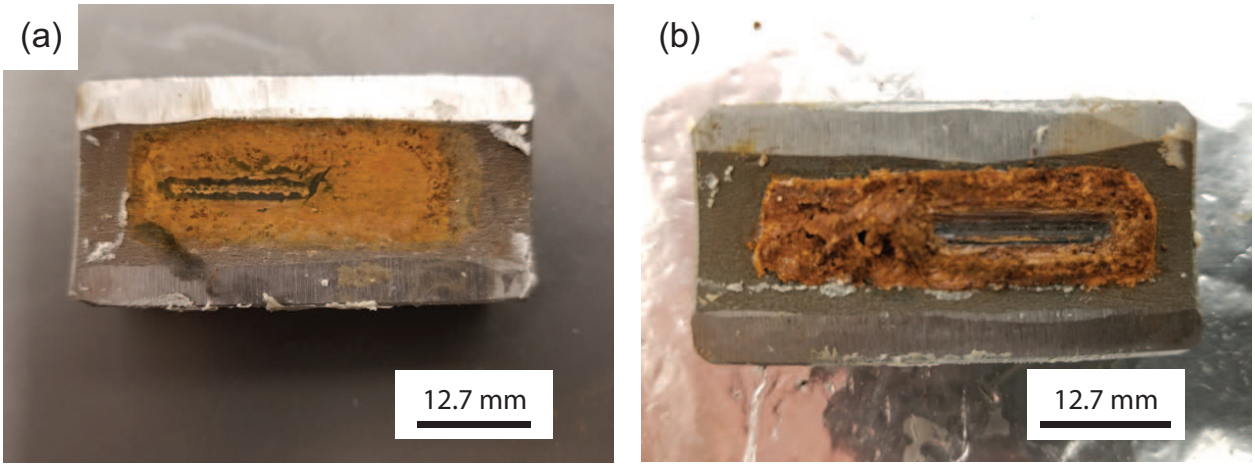

Figure 6.5: Pipe samples that have undergone tribocorrosion testing in high TDS water with DynaRate 6524 at 10 N load and 6 mm/s sliding velocity at an overpotential of (a) +10 mV and (b) +100 mV.

+10 mV overpotential, friction increased at an early onset from cycle 1000 onwards and also showed signs of fluctuations throughout. From Figure 6.5 (a) and (b), pictures of the samples taken afterwards show plenty of rust formation.

A second possible method to reduce the influence of corrosion that was investigated for the Calfrac project was the effect of CalGuard 3100 oxygen scavenger agent. CalGuard 3100 is sodium sulfite solution mixed into water at 10 %wt to 30 %wt. This additive is not typically used in high salinity water as it can form precipitates. With this in mind, we also wanted to know if it was miscible with high TDS water with DynaRate 6524 added, and if the friction reducer would continue to be effective. Friction testing was carried out with the same parameters as before this time with the addition of 1/2000 parts volume CalGuard 3100 as recommended for removing 9 ppm dissolved oxygen in water at room temperature. Figure 6.7 shows how added CalGuard 3100 effects the friction performance of DynaRate 6524. Figure 6.7 (a) shows that for no applied potential, without CalGuard 3100 the friction coefficient for the last 2500 cycles was $\mu = 0.085 \pm 0.003$, while with the presence of CalGuard 3100 $\mu = 0.083 \pm 0.003$, a nearly imperceptible change. However, from qualitative observations minor precipitates did appear and needed to be stirred back into the solution, and it was not completely clear whether this was salt or friction reducer that was amalgamating. Figure 6.7 (b) shows that for an overpotential of +100 mV, without CalGuard 3100 the friction coefficient is high and

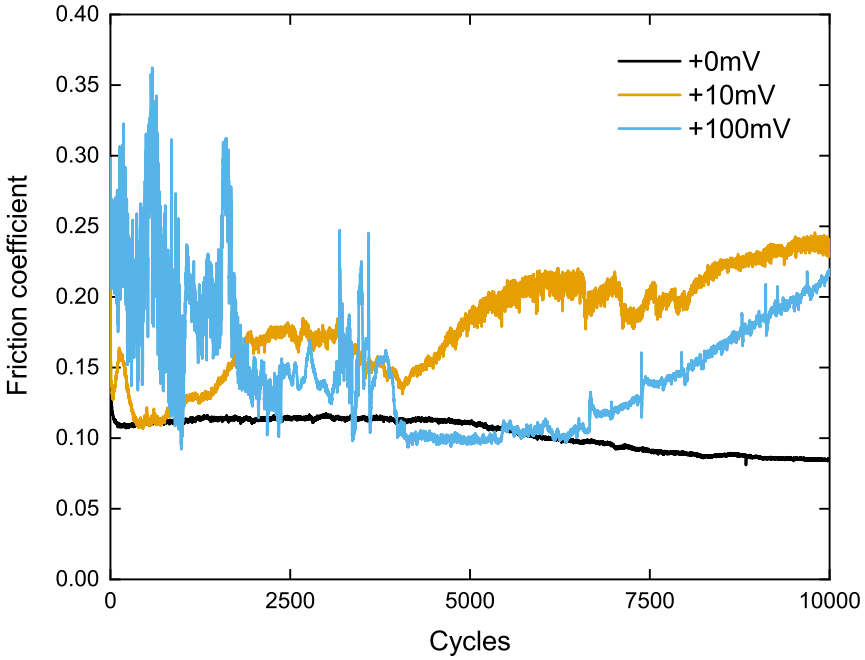

Figure 6.6: Friction coefficient versus cycle number of straight pipe for eletrocorrosion at various overpotentials in high TDS water with DynaRate 6524 at 10 N load and 6 mm/s sliding velocity.

quite unsteady and slopes upwards after 5000 cycles, while with the presence of CalGuard 3100 the friction coefficient for the last 2500 cycles was $\mu = 0.103 \pm 0.003$ and remained fairly steady all through the duration of the test.

6.4 Discussion

From the initial tests performed to compare the effect of friction reducers, it was identified that DynaRate 6524 was the most effective when it came down to reducing friction between the sapphire counter surface and steel pipe segment. From Figure 6.2, DynaRate 6524 lead to a 20% reduction in friction as compared to the baseline test without friction reducer, whereas DWP 621 resulted in an 20% increase in the friction coefficient and more unsteady friction behaviour. As mentioned, DynaRate is a cationic water-soluble polymer while DWP 621 is anionic. In general, anionic friction reducers are more cost effective, however, with increased suspended solids and salinity more expensive cationic friction reducers are required to tolerate high-salinity environments [97]. Although friction and wear are not directly related, reduced friction can be a sign of potentially reduced wear

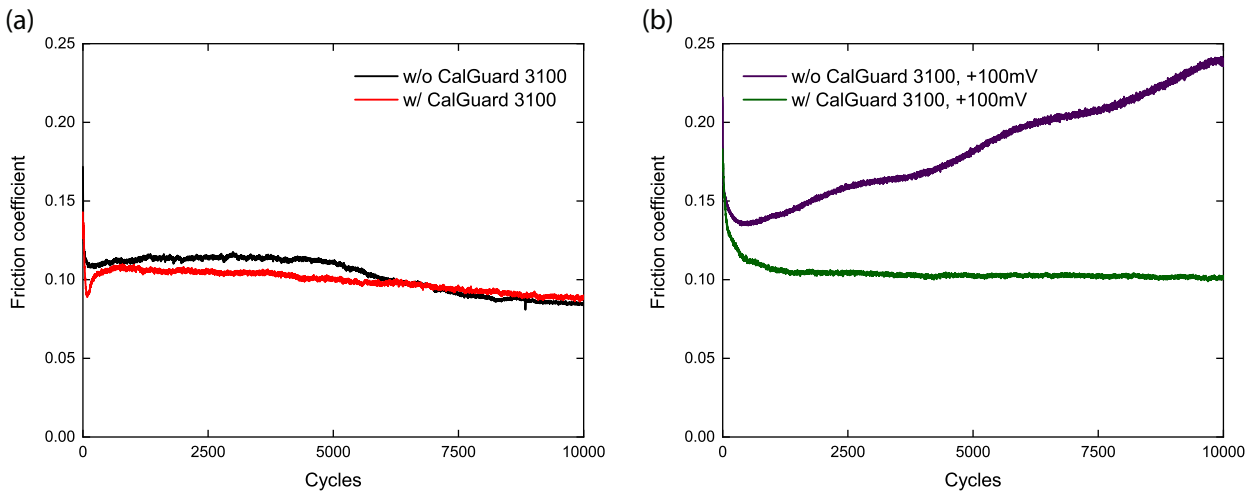

Figure 6.7: Friction coefficient versus cycle number of straight pipe in high TDS water with DynaRate 6524 at 10 N load and 6 mm/s sliding velocity without and with CalGuard 3100 with (a) no overpotential and (b) +100 mV overpotential.

which was observed. Pseudo-wear coefficients for straight pipe in high TDS water without friction reducer and DynaRate 6524 yielded similar results of $k = 1.11\times10^{-7} \pm 0.46\times10^{-7}$ and $k = 1.07\times10^{-7} \pm 0.40\times10^{-7}$ respectively, while DWP 621 exhibited much higher wear of $k = 1.85\times10^{-7} \pm 0.75\times10^{-7}$. However, we did note that in measuring the topography of the wear track using our optical profilometer that the curvature of the pipe did pose some issues regarding defining the edges of the wear scar. Also, from Figure 6.4 (c) it can be seen that the wear scar is not straight; although the path that the tribometer scraped along was indeed straight, variations in the roughness of the surface lead to a non-uniform wear scar. This increased the error of the calculated wear volume as seen in Figure 6.3. Although the main purpose of these friction reducers is to decrease frictional losses so as to decrease the pressures necessary to pump fracking fluid, there is the added benefit of reducing errosive wear under certain two-phase flow regimes [13, 95].

Figure 6.6 shows how the friction coefficient with the use of DynaRate 6524 in high TDS water is effected by artificially induced electrocorrosion. With no applied potential, the friction coefficient remained relatively steady for the duration of the test with an average friction coefficient from cycles 7500 to 10,000 of $\mu = 0.085 \pm 0.003$, while on the other hand friction was unsteady for induced electrocorrosion at +10 mV and +100 mV overpotentials, appearing to continue to increase beyond 10,000 cycles to over double the level

of with no overpotential. The selected overpontentials for the experiments were arbitrarily chosen given that Calfrac could not provide details on environmental operating conditions. From this information, we noted that corrosion is disadvantageous and prevented the DynaRate 6524 friction reducer from providing sufficient lubricity. In the high salinity environment, the ions are likely attaching together with the cationic friction reducer as we observed by the amalgamation of a thick precipitate near the surface of the water. Poor compatibility in high salinity environments is a common feature of all anionic friction reducers and even cationic friction reducers to a certain degree [98]. As a result, measures need to be taken to ensure that friction reducers remain suspended in solution or increased concentrations must be used.

In Figure 6.7, we looked at how friction coefficient with the use of DynaRate 6524 in high TDS water is effected by the use of CalGuard 3100 oxygen scavenger. As previously mentioned, CalGuard 3100 is not typically used in high salinity water as it can form precipitates. With the addition of this chemical at 1/2000 parts volume to the high TDS water, small precipitates could be observed with the naked eye, indicating that the DynaRate 6524 friction reducer could be compromised. Figure 6.7 (a) shows that for no overpotential the friction coefficient with and without the use of CalGuard 3100 remained unchanged. This indicates that the friction reducer was still effective even with the addition of the oxygen scavenger. However, with artificially induced electrocorrosion, at $^{+}$100 mV overpotential the friction coefficient rises once again showing that the friction reducer is ineffective. This time, the rise in friction coefficient is much more steady than before indicating that there is some sort of interaction between the friction reducer and the oxygen scavenger.

6.5 Conclusion

In short, DynaRate 6524 was found to be the most effective friction reducer for the steel pipe segments in high TDS water, decreasing friction by 20% while DWP 621 on the contrary hindered friction performance resulting in a 20% increase in friction. Wear was not significantly changed with the use of DynaRate 6524 but DWP 621 was found to be detrimental to wear performance. Electrocorrosion was found to have a negative

effect on the friction performance of DynaRate 6524, leading to increased and unsteady friction. Although CalGuard 3100 oxygen scavenger was found to be compatible with DynaRate 6524 with no applied potential, overpotentials lead to the same behaviour of DynaRate 6524 precipitating out of solution and becoming ineffective.

Chapter 7

Conclusions

The friction and wear performance of steel has been characterized using a home-built reciprocating tribometer. The home-built system was designed and constructed to perform experiments replicating the erosion-corrosion behaviour experienced by steel pipes under service conditions used in hydraulic fracturing. More specifically, an electrochemical fluid cell was constructed, such that the simultaneous impact of electrochemical corrosion, applied normal forces, and shearing forces on the corrosion rate and corrosion potential could be evaluated. The experimental apparatus developed showed good agreement with literature of dry sliding on steel surfaces against a ruby hemisphere. Furthermore, the tribometer showed sufficient sensitivity to detect changes in friction and wear under the influence of chemical potentials, friction modifiers and surface coatings.

Experiments evaluating the tribocorrosion resistance of boronized steels were conducted using the home-built tribometer. These boronized samples were proprietary samples acquired from Endurance Technologies Inc., and as such, the exact deposition process and chemical make-up of the surface layers were unknown. Significantly enhanced hardness, measured through both conventional microindentation and nanoindentation was observed at the surface of the steels. Polarization tests of the boronized steels also showed a decrease in the corrosive potential to more negative potentials compared with the conventional carbon steel samples. Several variants of the boronized steel samples were examined in the tribometer. A significant decrease in

both the wear rate and friction coefficient were observed for the boronized coating with additional boron-rich top layer. In samples that did not contain any additional boron doping, friction coefficients were similar to the carbon steel samples, but showed in every case a significant decrease in the amount of wear measured over the course of the experiment. Both the nitrogen-doped boronized steel and 316L stainless steel showed comparable friction coefficients when compared with the carbon steel sample. However, both samples showed a higher rate of wear than the carbon steel sample, suggesting they would not be good replacements for conventional carbon steel in erosion-corrosion applications. Tribocorrosion testing of the boron-doped steel sample, which had previously shown the best performance, showed that the friction coefficients were dependent on applied potentials which artificially induced corrosion; friction slightly decreased as the potential was increased. However, for untreated AISI 1018 steel, friction did not decrease as the potential was increased. Chemical analysis of the wear scars showed that the oxide was likely removed with each stroke of the tribometer counter surface, resulting in the inability of the surface to passivate. However, further analysis would be needed to gain further insight into the variance in friction and wear measured with applied potential.

In a second attempt to examine a second mechanism in which erosion corrosion rates can be controlled, the performance of AISI 4715 steel pipe sections cut directly from real pipes used in hydraulic fracturing were examined under real-world conditions. High salinity solutions taken from fracking sites were used for the corrosive medium in these experiments. Tribocorrosion experiments showed that the cationic friction modifiers outperformed anionic friction modifiers, which did not show significant improvement compared with solutions not containing any friction modifiers. An improvement in the wear rate was observed, although significant measurement error was associated with wear rates on these real pipe sections, resulting from the high roughness of the pipe sections. A significant decrease in the friction reducing performance of the cationic friction modifier was observed under electrically induced corrosion. However, when the oxygen was removed from the solution with an oxygen scavenger, the friction behaviour of the cationic friction modifier under electrically induced corrosion was slightly altered resulting in steadier friction performance over time.

In summary, friction performance of steels under corrosive conditions can be enhanced through both surface modification and the addition of friction modifiers in the corrosive solution. Doping surface slightly can also significantly impact the friction and wear performance of the coating. Finally, the corrosive potential can also impact the performance of either coatings or modifiers, suggesting that examination of cathodic protection or other modification of the potential of the steel can influence both friction and corrosive rates.

Chapter 8

Future Work

In this thesis, a home-built reciprocating tribometer was created for the testing of steel samples in order to evaluate their friction and wear performance under different conditions both dry and corrosive aqueous environments. Parts including linear stages and force/torque sensor were specifically selected for proposed friction experiments. More focus was devoted to determining the friction and wear coefficients for dry sliding, and only friction coefficients were obtained for wet sliding in corrosive environments. Wear was much lower in these wet environments, and as a result it was much harder to accurately determine wear coefficients. Due to the short duration of these wet tests and low loads which had to be applied in order to maintain realistic contact pressures, wear scars were shallow and had similar surface roughness as regions outside the wear scar making them hard to discern. In order to achieve sufficiently measurable wear volumes, some of these tests would otherwise have had to run over several days. For future work, running longer tests would enabled us to compare the volume lost due to both corrosion and erosion occurring simultaneously, to the volume lost due to corrosion alone without the effects of erosion. In future work studying the behaviour of steel samples under tribocorrison, it may also be advantageous to change the geometry of the counter surface as to improve the accuracy of measured wear volumes. Besides our Zeta-20 optical profiler, other tools have been looked into for surface metrology including white light interferometers with a large field of view that do not require image

stitching, and contact metrology tools such as SPM imaging. One of the greatest challenges encountered when measuring wear volumes was discerning where the wear scar edge begins and ends. With improved software, rather than just using contrast-based recognition with no filtering, boundaries for wear scars could be better identified. In addition to determining pseudo-wear coefficients for the given steel samples in Chapter 5, more micro- and nanohardness tests could be performed on other samples in the future so as to obtain real wear coefficients for all samples. Also, instead of using a Vickers tip for microhardness testing a Knoops tip could be used which has been suggested for thin coatings such as those used in these studies.

For the tribocorrosion studies carried out in Chapter 6, a number of improvements could be made to our experiments. During these tests, friction was monitored however, it would have been advantageous to simultaneously measure changes in the current coming off of the sample as to associate minor changes in friction to changing in chemical reactions occurring at the same time. We could also measure the pH of the high TDS water to identify the role it plays in tribocorrosion along with the resistivity of the water so as to better estimate the salinity. Also, in performing tribocorrosion experiments, it would have been nice to have also been able to perform the same tests on all the other boronized steel samples and stainless steel, however, this was not possible within our time constraints. The chemical characterisation technique that we employed was EDS. This technique was only able to determine the elemental composition to a certain degree (as quantisation of boron was poor), and could not determine chemical compounds formed. Instead for future studies, I would advise moving forward with X-ray Photoelectron Spectroscopy (XPS) because of its ability to characterise both elements and chemical bonds, and higher signal to noise ratio for light elements ($Z > 3$) that EDS has troubles with identifying. With XPS, we would hope to confirm whether our hypothesis holds true that the wearing of a thin oxide film on the surface leads to a the production of a friction reducing tribofilm. As a final note, if possible it may also be advantageous to measure the worn volume of the sapphire counter surface to determine the actual contact area and contact pressures present during sliding.

Bibliography

[1] K. Holmberg and A. Erdemir, "Influence of tribology on global energy consumption, costs and emissions," *Friction*, vol. 5, pp. 263–284, sep 2017.

[2] M. Bauccio and American Society for Metals., *ASM metals reference book*. ASM International, 1993.

[3] J. D. B. de Mello, W. S. Labiapari, M. A. N. Ardila, S. A. G. Oliveira, and H. L. Costa, "Strain Hardening: Can it Affect Abrasion Resistance?," *Tribology Letters*, vol. 65, p. 67, jun 2017.

[4] D. Patel, V. Jain, and J. Ramkumar, "Micro texturing on metallic surfaces: State of the art," *Proceedings of the Institution of Mechanical Engineers, Part B: Journal of Engineering Manufacture*, vol. 232, pp. 941–964, aug 2016.

[5] E. Medvedovski, J. R. Jiang, and M. Robertson, "Tribological properties of boride based thermal diffusion coatings," *Advances in Applied Ceramics*, vol. 113, pp. 427–437, oct 2014.

[6] R. S. Petrova, N. Suwattananont, and V. Samardzic, "The effect of boronizing on metallic alloys for automotive applications," *Journal of Materials Engineering and Performance*, vol. 17, no. 3, pp. 340–345, 2008.

[7] J. Rus, C. Luis De Leal, and D. N. Tsipas, "Boronizing of 304 steel," *Journal of Materials Science Letters*, vol. 4, no. 5, pp. 558–560, 1985.

[8] D. S. Xu, X. Xu, Z. G. Su, J. An, and Y. Lu, "Mechanical properties, wear, and corrosion of boronized N80 tube steel," *Materials Science*, vol. 48, no. 1, pp. 106–112, 2012.

[9] R. H. Biddulph, "Boronizing for erosion resistance," *Thin Solid Films*, vol. 45, no. 2, pp. 341–347, 1977.

[10] A. Hedayata, S. Yannacopoulosa, and J. Postlethwaiteb, "Wear and CO2 corrosion of steel couplings and tubing in heavy oil screw-pump wells," *Wear*, vol. 209, pp. 263–273, aug 1997.

[11] P. Ko, K. Humphreys, and C. Matthews, "Reciprocating-sliding wear of sucker rods and production tubing in deviated oil wells," *Wear*, vol. 134, pp. 13–28, nov 1989.

[12] R. Mottram, "Sucker Rod Wear In Directionally Drilled Steamflood Wells," *Journal of Canadian Petroleum Technology*, vol. 30, mar 1991.

[13] I. Hutchings, "Wear by particulates," *Chemical Engineering Science*, vol. 42, pp. 869–878, jan 1987.

[14] T. Mang, K. Bobzin, and T. Bartels, *Industrial Tribology: Tribosystems, Friction, Wear and Surface Engineering, Lubrication*. Wiley-VCH, 2011.

[15] A. A. Pitenis, D. Dowson, and W. Gregory Sawyer, "Leonardo da Vinci's Friction Experiments: An Old Story Acknowledged and Repeated," *Tribology Letters*, vol. 56, pp. 509–515, dec 2014.

[16] W. J. Bartz, "History of Tribology - the Bridge Between the Classical Antiquity and the 21st Century," tech. rep., 2001.

[17] K. T. Reye and K. R. Bornemann, "Zur Theorie der Zapfenreibung," *Der Civilingenieur - Zeitschrift für das Ingenieurwesen*, 1860.

[18] J. F. Archard, "Contact and Rubbing of Flat Surfaces," *Journal of Applied Physics*, vol. 24, pp. 981–988, aug 1953.

[19] B. Bhushan, *Modern Tribology Handbook*. CRC Press, dec 2001.

[20] A. Shebani and C. Pislaru, "Wear Measuring and Wear Modelling Based on Archard, ASTM, and Neural Network Models," *International Journal of Mechanical, Aerospace, Industrial and Mechatronics Engineering*, vol. 9, pp. 177–182, jan 2015.

[21] J. W. Gibbs and W. Translated by Ostwald, "Thermodynamische Studien," *Nature*, vol. 46, jul 1892.

[22] W. Nernst, "Die elektromotorische Wirksamkeit der Jonen," *Zeitschrift für Physikalische Chemie*, vol. 4U, pp. 129–181, jul 1889.

[23] L. J. Korb, *Corrosion*. ASM International, 1987.

[24] P. R. Roberge, *Corrosion engineering: principles and practice*. New York: McGraw-Hill Education, 2008.

[25] M. Faraday, "The Fundamental Laws of Electrolytic Conduction," in *Experimental Researches in Electricity*, pp. 102–147, 1833.

[26] J. Tafel, "Über die Polarisation bei kathodischer Wasserstoffentwicklung," *Zeitschrift für Physikalische Chemie*, vol. 50U, pp. 641–712, jan 1905.

[27] A. D.-A. Jenson, "The evolution of hardness and tribofilm growth during running-in of case carburized steel under boundary lubrication Recommended Citation The evolution of hardness and tribofilm growth during running-in of case carburized steel under boundary lubrication," tech. rep., 2017.

[28] A. Akchurin and R. Bosman, "A Deterministic Stress-Activated Model for Tribo-Film Growth and Wear Simulation," *Tribology Letters*, vol. 65, p. 59, jun 2017.

[29] P. Jemmely, S. Mischler, and D. Landolt, "Electrochemical modeling of passivation phenomena in tribocorrosion," *Wear*, vol. 237, pp. 63–76, jan 2000.

[30] S. Mischler and P. Ponthiaux, "A round robin on combined electrochemical and friction tests on alumina/stainless steel contacts in sulphuric acid," *Wear*, vol. 248, pp. 211–225, mar 2001.

[31] S. Mischler, A. Spiegel, M. Stemp, and D. Landolt, "Influence of passivity on the tribocorrosion of carbon steel in aqueous solutions," *Wear*, vol. 251, pp. 1295–1307, oct 2001.

[32] M. Stemp, S. Mischler, and D. Landolt, "The effect of contact configuration on the tribocorrosion of stainless steel in reciprocating sliding under potentiostatic control," *Corrosion Science*, vol. 45, pp. 625–640, mar 2003.

[33] L. Pinder, K. Dawson, and G. Tatlock, "High Temperature Corrosion of Low Alloy Steels," in *Shreir's Corrosion*, pp. 558–582, Elsevier, jan 2010.

[34] S. Hassani, K. P. Roberts, S. A. Shirazi, J. R. Shadley, E. F. Rybicki, and C. Joia, "Flow loop study of NaCl concentration effect on erosion, corrosion, and erosion-corrosion of carbon steel in CO 2-saturated systems," *Corrosion*, vol. 68, feb 2012.

[35] R. Khan, H. H. Ya, W. Pao, and A. Khan, "Erosion–Corrosion of 30°, 60°, and 90° Carbon Steel Elbows in a Multiphase Flow Containing Sand Particles," *Materials*, vol. 12, p. 3898, nov 2019.

[36] B. Bozzini, M. E. Ricotti, M. Boniardi, and C. Mele, "Evaluation of erosion-corrosion in multiphase flow via CFD and experimental analysis," *Wear*, vol. 255, no. 1-6, pp. 237–245, 2003.

[37] R. J. Wood, T. F. Jones, J. Ganeshalingam, and N. J. Miles, "Comparison of predicted and experimental erosion estimates in slurry ducts," *Wear*, vol. 256, pp. 937–947, may 2004.

[38] H. Zhang, S. Liu, and H. Xiao, "Tribological properties of sliding quartz sand particle and shale rock contact under water and guar gum aqueous solution in hydraulic fracturing," *Tribology International*, vol. 129, pp. 416–426, jan 2019.

[39] Y. Zhang, X. Zhang, and G. Matsoukas, "Numerical study of surface texturing for improving tribological properties of ultra-high molecular weight polyethylene," *Biosurface and Biotribology*, vol. 1, pp. 270–277, dec 2015.

[40] D. Toboła, W. Brostow, K. Czechowski, and P. Rusek, "Improvement of wear resistance of some cold working tool steels," *Wear*, vol. 382-383, pp. 29–39, jul 2017.

[41] A. F. Zhigach, I. S. Antonov, M. A. Pchelkina, G. I. Yukin, A. S. Dobrodeev, and V. N. Matveev, "Surface impregnation of steel with boron from the gas phase," *Metal Science and Heat Treatment of Metals*, vol. 1, no. 4, pp. 47–50, 1959.

[42] W. Fichtl, "Boronizing and its practical applications," *Materials and Design*, vol. 2, no. 6, pp. 276–286, 1981.

[43] Norris, "Sucker Rod Failure Analysis," tech. rep., 2015.

[44] M. J. Schneider, M. S. Chatterjee, and Bodycote, "Introduction to Surfaec Hardening of Steels," in *ASM Handbook* (J. Dossett and G. E. Totten, eds.), ch. Steel Heat, pp. 389–398, ASM International, 4a ed., 2013.

[45] J. R. Davis, *Surface hardening of steels : understanding the basics*. ASM International, 2002.

[46] C. Zimmerman, "Boriding (Boronizing) of Metals," in *Steel Heat Treating Fundamentals and Processes*, pp. 709–724, ASM International, 2013.

[47] Y. Kayali, A. Büyüksaçiş, and Y. Yalçin, "Corrosion and wear behaviors of boronized AISI 316L stainless steel," *Metals and Materials International*, vol. 19, no. 5, pp. 1053–1061, 2013.

[48] J. Subrahmanyam and K. Gopinath, "Wear studies on boronized mild steel," *Wear*, vol. 95, no. 3, pp. 287–292, 1984.

[49] L. Gandossi, "An overview of hydraulic fracturing and other formation stimulation technologies for shale gas production," tech. rep., 2013.

[50] M. Lallanilla, "Facts About Fracking," 2018.

[51] R. Jackson, A. Gorody, B. Mayer, J. Roy, M. Ryan, and D. Van Stempvoort, "Groundwater Protection and Unconventional Gas Extraction: The Critical Need for Field-Based Hydrogeological Research," *Groundwater*, vol. 51, pp. 488–510, jul 2013.

[52] Frac Focus, "Fracturing Fluid Management," 2019.

[53] J. E. Johnston, E. Werder, and D. Sebastian, "Wastewater Disposal Wells, Fracking, and Environmental Injustice in Southern Texas.," *American journal of public health*, vol. 106, pp. 550–6, mar 2016.

[54] BBC News, "Fracking in Lancashire: Second 0.8 tremor in 24 hours," 2018.

[55] H. Kaleli, "Tribology in Industry New Universal Tribometer as Pin or Ball-on-Disc and Reciprocating Pin-on-Plate Types," *Tribology in Industry*, vol. 38, no. 2, pp. 235–240, 2016.

[56] D. L. Burris and W. G. Sawyer, "Addressing Practical Challenges of Low Friction Coefficient Measurements," *Tribology Letters*, vol. 35, pp. 17–23, jul 2009.

[57] T. L. Schmitz, J. E. Action, J. C. Ziegert, and W. G. Sawyer, "The Difficulty of Measuring Low Friction: Uncertainty Analysis for Friction Coefficient Measurements," *Journal of Tribology*, vol. 127, no. 3, p. 673, 2005.

[58] S. Tehrani, "Are there any disadvantages for using reciprocating wear test in high speed?," 2019.

[59] E. Ivanov, I. Borovanska, B. Milosheva, and R. Kotsilkova, "Experimental Nano and Micro Mechanics of Nanostructured Materials," in *Mechanics of Nanomaterials and Nanotechnology*, ch. Chapter 3, pp. 287–326, Dordrecht: Springer, 2012.

[60] P. Leroux and D. Li, "Continuous Stribeck Curve Measurement Using Pin-on-Disk Tribometer," tech. rep., 2012.

[61] ATI Industrial Automation, "ATI Industrial Automation: F/T Sensor Mini40," 2019.

[62] National Instruments, "63xx Models : DAQ Multifunction I/O Cable and Accessory Compatibility - National Instruments," 2019.

[63] K. Johnson, *Contact Mechanics*. Cambridge, United Kingdom: Cambridge University Press, 1987.

[64] L. Joly-Pottuz, "Nanolubricants," in *Encyclopedia of Tribology* (Q. J. Wang and Y.-W. Chung, eds.), p. 228, Boston, MA: Springer US, 2013 ed., 2013.

[65] T. Reddyhoff, A. Schmidt, and H. Spikes, "Thermal Conductivity and Flash Temperature," *Tribology Letters*, vol. 67, p. 22, mar 2019.

[66] InStock901, "EG&G / Princeton Applied Research Potentiostat Galvanostat Model 273. inStock901.com - Technology Superstore of BPAI LLC," 2019.

[67] J. Zhong, W. Qin, X. Wang, E. Medvedovski, J. A. Szpunar, and K. Guan, "Mechanism of Texture Formation in Iron Boride Coatings on Low-Carbon Steel," *Metallurgical and Materials Transactions A*, vol. 50, pp. 58–62, jan 2019.

[68] F. J. Millero, R. Feistel, D. G. Wright, and T. J. McDougall, "The composition of Standard Seawater and the definition of the Reference-Composition Salinity Scale," *Deep Sea Research Part I: Oceanographic Research Papers*, vol. 55, pp. 50–72, jan 2008.

[69] ASTM, "ASTM G59-97(2014) Standard Test Method for Conducting Potentiodynamic Polarization Resistance Measurements," in *ASTM International*, West Conshohocken, PA: ASTM, 2017 ed., 2014.

[70] Polytec, "The Basics of White Light Interferometry," 2017.

[71] KLA, "Zeta-20 Optical Profiler — Surface Profilers — KLA," 2019.

[72] D. B. Williams and B. C. Carter, *Transmission Electron Microscopy: A Textbook for Materials Science*. New York, NY: Plenum Press, 2004.

[73] CCWJ, "Microscopy," 2012.

[74] ASTM, "ASTM E384-17 Standard Test Method for Microindentation Hardness of Materials," in *ASTM International*, West Conshohocken, PA: ASTM International, 2017 ed., 2017.

[75] T. Sanponpute and A. Meesaplak, "Vibration effect on hardness measurement," *Measurement*, vol. 43, pp. 631–636, jun 2010.

[76] R. Smallman, A. Ngan, R. Smallman, and A. Ngan, *Modern Physical Metallurgy*. Butterworth-Heinemann, jan 2014.

[77] I. International, "ISO 14577-1:2015 - Metallic materials - Instrumented indentation test for hardness and materials parameters," in *ISO Standards*, Geneva: ISO International, 2015.

[78] SURFACE Nanolab, "Nanoindenter tips," 2019.

[79] E. Broitman, "Indentation Hardness Measurements at Macro-, Micro-, and Nanoscale: A Critical Overview," *Tribology Letters*, vol. 65, 2017.

[80] P. Kuisma-Kursula, "Accuracy, precision and detection limits of SEM-WDS, SEM-EDS and PIXE in the multi-elemental analysis of medieval glass," *X-Ray Spectrometry*, vol. 29, pp. 111–118, jan 2000.

[81] Carl Zeiss Microscopy GmbH, "Low Loss Backscattered Electron (BSE) Imaging - Principles and Advantages Using GEMINI Technology," 2010.

[82] NIST Physical Measurement Laboratory, "X-ray Transition Energies Database," 2019.

[83] D. Klenam, C. Polese, L. Chown, S. Kwofie, and L. Cornish, "Mechanical behaviour of pack carburized AISI 316L austenitic stainless steel," *Journal of the Southern African Institute of Mining and Metallurgy*, vol. 115, no. 12, pp. 1183–1191, 2015.

[84] S. Mudhivarthi, *Dry sliding tribological characteristics of hard, flat materials with low surface roughness*. PhD thesis, Univeristy of South Florida, 2003.

[85] AZoMaterials, "AISI 4140 Alloy Steel (UNS G41400)," 2012.

[86] Otai Special Steel, "ASTM 52100 Bearing Steel," 2019.

[87] J. Sugimura, B. Ono, M. Hashimoto, H. Tanaka, and Y. Yamamoto, "Sliding experiments of steels in gaseous hydrogen," *Tribology and Interface Engineering Series*, vol. 48, pp. 465–473, jan 2005.

[88] A. K. Vijh, "The influence of metal-metal bond energies on the adhesion, hardness, friction and wear of metals," *Journal of Materials Science*, vol. 10, pp. 998–1004, jun 1975.

[89] F. A. Cotton, G. Wilkinson, C. A. Murillo, and M. Bochmann, *Advanced inorganic chemistry.* Wiley-Interscience, 1999.

[90] C. Martini, G. Palombarini, G. Poli, and D. Prandstraller, "Sliding and abrasive wear behaviour of boride coatings," *Wear*, vol. 256, pp. 608–613, mar 2004.

[91] S. Sen, U. Sen, and C. Bindal, "Tribological properties of oxidised boride coatings grown on AISI 4140 steel," *Materials Letters*, vol. 60, pp. 3481–3486, dec 2006.

[92] S. Hulikal, N. Lapusta, and K. Bhattacharya, "Static and sliding contact of rough surfaces: Effect of asperity-scale properties and long-range elastic interactions," *Journal of the Mechanics and Physics of Solids*, vol. 116, pp. 217–238, jul 2018.

[93] I. J. Ford, "Roughness effect on friction for I multi-asperity contact between surfaces I," tech. rep., 1993.

[94] Steel Grades, "Steel GradeAISI 4715 Chemical information, Mechanical properties," tech. rep., 2019.

[95] S. Khan, L. Shen, and N. Everson, "Engineered Friction Reducers Enhance Proppant Transport," 2018.

[96] CalFrac Well Services, "DWP 621 Material Safety Data Sheet," 2019.

[97] J. Fichter, A. Bui, G. Grawunder, and T. Jones, "Critical Considerations for Successful Hydraulic Fracturing and Shale Gas Recovery," tech. rep., 2010.

[98] T. C. Nguyen, B. Romero, E. Vinson, and H. Wiggins, "Effect of salt on the performance of drag reducers in slickwater fracturing fluids," *Journal of Petroleum Science and Engineering*, vol. 163, pp. 590–599, apr 2018.